

Effect of Planetary Rotation on Oceanic Surface Boundary Layer Turbulence

JINLIANG LIU AND JUN-HONG LIANG^{a,b}

Department of Oceanography and Coastal Sciences, Louisiana State University, Baton Rouge, Louisiana

JAMES C. MCWILLIAMS

Department of Atmospheric and Oceanic Science, University of California, Los Angeles, Los Angeles, California

PETER P. SULLIVAN

National Center for Atmospheric Research, Boulder, Colorado

YALIN FAN

Oceanography Division, Naval Research Laboratory, Stennis Space Center, Mississippi

QIN CHEN

Department of Civil and Environmental Engineering, Northeastern University, Boston, Massachusetts

(Manuscript received 29 July 2017, in final form 9 May 2018)

ABSTRACT

A large-eddy simulation (LES) model is configured to investigate the effect of the horizontal (northward) component of Earth's rotation f_h on upper-ocean turbulence. The focus is on the variability of the f_h effect with latitude/hemisphere in the presence of surface gravity waves and when capped by a stable stratification beneath the surface layer. When f_h is included, the mean flow, turbulence, and vertical mixing depend on the wind direction. The value and effect of f_h are the largest in the tropics and decrease with increasing latitudes. The variability in turbulent flows to wind direction is different at different latitudes and in opposite hemispheres. When limited by stable stratification, the variability in turbulence intensity to wind direction reduces, but the entrainment rate changes with wind direction. In wave-driven Langmuir turbulence, the variability in mean current to wind direction is reduced, but the variability of turbulence to wind direction is evident. When there is wind-following swell, the variability in the mean current to wind direction is further reduced. When there is strong wind-opposing swell so that the total wave forcing is opposite to the wind, the variability in the mean current to wind direction is reduced, but the variability of turbulence to wind direction is enhanced, compared to in Ekman turbulence. The profiles of eddy viscosity, including its shape and its value, show a strong wind direction dependence for both stratified wind-driven and wave-driven Langmuir turbulence. Our study demonstrates that wind direction is an important parameter to upper-ocean mixing, though it is overlooked in existing ocean models.

1. Introduction

Turbulent flows in the oceanic surface boundary layer (OSBL) are important to Earth's climate and marine

environment. They control the air-sea exchange of heat, momentum, and trace materials. They also determine the transport, dispersion, and transformation of materials such as nutrients, larvae, and pollutants in the upper ocean. OSBL turbulence is driven by surface atmospheric (or meteorological) conditions including winds, waves, and heat fluxes and is modulated by stratification and the rotation of Earth. While the effect of different surface meteorological conditions on OSBL turbulence has been relatively well studied through a series of observation programs (e.g., Price et al. 1978; Weller and

^a Additional affiliation: Center for Computation and Technology, Louisiana State University, Baton Rouge, Louisiana.

^b Additional affiliation: Coastal Studies Institute, Louisiana State University, Baton Rouge, Louisiana.

Corresponding author: Jun-Hong Liang, jliang@lsu.edu

Price 1988; Smith 1992; Plueddemann et al. 1996; Gargett et al. 2004; Fer 2006; Sanford et al. 2011; D'Asaro 2014; D'Asaro et al. 2014) and numerical studies (e.g., Skillingstad and Denbo 1995; McWilliams et al. 1997; Li et al. 2005; Belcher et al. 2012), the effect of Earth's rotation, particularly its horizontal component, is relatively less studied and is insufficiently understood.

Studying the effect of planetary rotation on OSBL dates back to the seminal work by Ekman (1905), who derived analytic solutions for the mean horizontal current in OSBL, known as the Ekman spiral, under the influence of a steady uniform surface wind and the vertical component of Earth's rotation ($f = 2\Omega \sin\phi$, where Ω is the angular speed of Earth's rotation, and ϕ is the latitude). The Ekman theory successfully explains the wind-driven transport at the surface; however, recent studies (e.g., Price and Sundermeyer 1999) have demonstrated discrepancies between observed velocity profiles with Ekman's solutions.

The horizontal component ($f_h = 2\Omega \cos\phi$) of planetary rotation is neglected in the momentum equation in circulation models because it is small compared to other terms, such as the Coriolis force and pressure gradient term in the momentum budgets (White and Bromley 1995). However, recent studies (Etling and Wippermann 1975; Leibovich and Lele 1985; Garwood et al. 1985a,b; Galperin et al. 1989; Kantha et al. 1989; Coleman et al. 1990; Hassid and Galperin 1994; Wang et al. 1996; Zikanov et al. 2003; McWilliams and Huckle 2006; Wang 2006) reveal that f_h alters the mean horizontal velocity as well as vertical mixing in the OSBL.

Through a series of linear stability analyses, Etling and Wippermann (1975) and Leibovich and Lele (1985) showed that the horizontal component of planetary rotation can act as a destabilizing agent in the planetary Ekman layer by enlarging the bands of unstable wavenumbers and thereby reducing the critical Reynolds number.

Using a bulk mixed layer model, Garwood et al. (1985a,b) suggested that the interaction between Reynolds stress and horizontal component of planetary rotation influences the conversion of turbulent kinetic energy (TKE) between horizontal and vertical components. They hypothesized that the horizontal component of Earth's rotation, together with wind and buoyancy, induces a deeper mixed layer in the western tropical Pacific and a shallower mixed layer in the eastern tropical Pacific.

Using the level 2.5 second-order turbulence closure model (Mellor and Yamada 1982), Galperin et al. (1989) and Kantha et al. (1989) examined the impact of the horizontal component of Earth's rotation on turbulent mixing in stably stratified, shear-driven turbulent flows near the equator and concluded that the effect of f_h on mixed layer depth (MLD) is small due to the stable stratification.

However, Hassid and Galperin (1994) found that the effects of Earth's rotation (both horizontal and vertical components) can be significant under neutral and unstable stratification.

More recently, the f_h effect on OSBL turbulence was studied using turbulence-resolving models. In a direct numerical simulation (DNS) study of the turbulent atmospheric Ekman layer with neutral stratification, Coleman et al. (1990) showed that the wind direction led to 6% variations in the surface friction velocity and 9° difference in the maximum and minimum of the angle between the wall shear stress and the free-stream velocity at 45°N. Using a large-eddy simulation (LES) model, Wang et al. (1996) extended the bulk mixed layer model to include entrainment and found that the effect of f_h on OSBL turbulent mixing at the equator is small when entraining heat flux is significant. In a subsequent study, Wang (2006) found that the effect of f_h on turbulent convection at 60°N is also small.

Zikanov et al. (2003) revisited the classic Ekman theory and investigated the flow dependence on latitude and wind direction by considering a turbulent shear flow driven by a steady surface wind using an LES model. They showed that both the mean current and the turbulence change with wind direction due to f_h , and the effect increases with decreasing latitudes. They demonstrated that wind direction exerts a nonnegligible impact on wind-driven Ekman turbulence due to the horizontal (northward) component of Earth's rotation: turbulence is enhanced when the wind has a westward and southward component and is suppressed when the wind has an eastward and northward component in the absence of other processes in the Northern Hemisphere.

However, to the best of our knowledge, no study has systematically investigated the influence of three possibly important factors: hemisphere, stable stratification below the mixed layer, and nonbreaking surface gravity waves. Hemisphere is a nonnegligible factor when studying the effect of rotation on OSBL turbulence. It affects the direction of the Coriolis force, which limits the evolution of turbulence, since the vertical rotation is reversed in opposite hemispheres. At low to midlatitudes where f_h is relatively large, the mixed layer is relatively shallow due to strong surface heating. Stable stratification below the mixed layer suppresses the development of turbulence and traps the Ekman transport within a relatively shallow mixed layer, which also limits the exchange of materials inside and outside the boundary layer. Surface gravity waves are ubiquitous over the global ocean. They drive coherent Langmuir circulations (LCs; or Langmuir turbulence) that modify the mean currents, mixing, and dissipation profiles (e.g., Sullivan et al. 2007; Belcher et al. 2012). LCs were first observed by Langmuir (1938), later

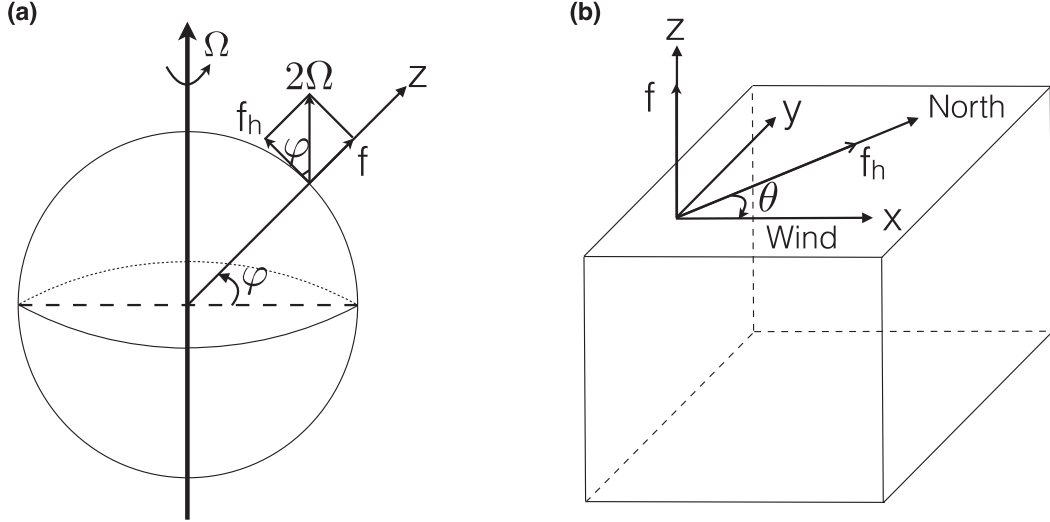


FIG. 1. Sketch of (a) planetary rotation: planetary rotation vector Ω , Coriolis parameter f , and horizontal component of planetary rotation f_h ; (b) domain orientation: latitude φ , and θ is the angle from the northward direction to the downwind direction in a clockwise rotation sense; x axis is aligned with wind stress.

theoretically modeled by Craik and Leibovich (1976), and more recently studied numerically via the LES of the Craik–Leibovich equations (e.g., McWilliams et al. 1997; Li et al. 2005; Tejada-Martínez and Grosch 2007; Harcourt and D’Asaro 2008; Pearson et al. 2015).

The objectives of this study are 1) to expand the analysis of turbulent Ekman flow under the influence of f_h , 2) to study the variability of the f_h effect for varying latitude and hemisphere, and 3) to investigate how the addition of nonbreaking surface gravity waves and stratification modify the effect of f_h . The objectives are achieved by analyzing a series of solutions from a large-eddy simulation model. The rest of the paper is organized as follows. Section 2 presents the theoretical background necessary for understanding of the effect of f_h on upper-ocean turbulence. Section 3 describes the LES model and model configuration. Section 4 presents the numerical solutions and explores the effect of f_h on the depth of OSBL, eddy viscosity profile, TKE production, TKE dissipation, and residence time of TKE in the absence of stratification and surface gravity waves, and it also describes the latitude/hemisphere dependence of the f_h effect and the modification of the f_h effect due to stratification, Langmuir turbulence, swell, and the combination of stratification and waves. Section 5 discusses the effect of f_h on eddy viscosity profiles. Section 6 is a discussion and summary.

2. Background theory

The effect of f_h on turbulence can be understood by the TKE and the momentum flux budget equations. Following Zikanov et al. (2003), the equations are

$$\frac{1}{2} \frac{\partial \langle u'^2 \rangle}{\partial t} = -f_{hy} \langle u' w \rangle + \dots, \quad (1)$$

$$\frac{1}{2} \frac{\partial \langle v'^2 \rangle}{\partial t} = f_{hx} \langle v' w \rangle + \dots, \quad (2)$$

$$\frac{1}{2} \frac{\partial \langle w^2 \rangle}{\partial t} = f_{hy} \langle u' w \rangle - f_{hx} \langle v' w \rangle + \dots, \quad (3)$$

$$\frac{\partial \langle u' w \rangle}{\partial t} = f_{hy} (\langle u'^2 \rangle - \langle w^2 \rangle) + \dots, \quad \text{and} \quad (4)$$

$$\frac{\partial \langle v' w \rangle}{\partial t} = -f_{hx} (\langle v'^2 \rangle - \langle w^2 \rangle) + \dots, \quad (5)$$

where u , v , and w are the components of velocities in x (downwind), y (crosswind), and z (positive upward) directions, respectively (i.e., the equations are in the wind coordinate; see Fig. 1). A horizontal mean is denoted by angle brackets $\langle \rangle$, and a deviation from the horizontal mean is denoted by prime (for a variable X , $X = \langle X \rangle + X'$). Other variables that appear in the above equations are the horizontal component f_h of Earth’s rotation vector projected in x ($f_{hx} = 2\Omega \cos\varphi \cos\theta$) and y ($f_{hy} = 2\Omega \cos\varphi \sin\theta$) directions, where θ is the angle measured from the northward direction (the direction of f_h) to the downwind direction in a clockwise sense (e.g., northward wind for $\theta = 0^\circ$). The dots on the right-hand side (RHS) of Eqs. (1)–(5) represent other terms, including shear production, turbulent transport, the Coriolis effects associated with the vertical component of planetary rotation, buoyancy, production/destruction due to Stokes vortex force, and pressure transport (McWilliams et al. 2012) that are identical to when $f_h = 0$.

The horizontal component of Earth's rotation affects OSBL turbulence in two ways: 1) through the redistribution of turbulent kinetic energy between horizontal and vertical directions and 2) through the modification of the vertical momentum fluxes ($\langle u'w \rangle$ and $\langle v'w \rangle$) (e.g., Zikanov et al. 2003). While the sign of terms f_h in the budget equation of a variable does not imply the increase or decrease of the variable, Zikanov et al. (2003) showed that for an unstratified Ekman layer, $\langle u'w \rangle$ is more negative, $\langle v'w \rangle$ is more positive, and volume-averaged TKE increases when both f_{hx} and f_{hy} are negative ($180^\circ < \theta < 270^\circ$). In contrast, $\langle u'w \rangle$ is less negative, $\langle v'w \rangle$ is less positive, and volume-averaged TKE decreases when both f_{hx} and f_{hy} are positive ($0^\circ < \theta < 90^\circ$) in the Northern Hemisphere (see Figs. 8a,b, 9a in Zikanov et al. 2003).

3. Model description and configuration

a. Model description

The model used in the study is the National Center for Atmospheric Research (NCAR) LES model for a wave-driven oceanic boundary layer (McWilliams et al. 1997; Sullivan and McWilliams 2010), with the addition of the horizontal component of planetary rotation. The filtered (i.e., LES) Craik–Leibovich equations for momentum in a Cartesian coordinate system with Earth's rotation are (e.g., McWilliams et al. 1997; Moeng and Sullivan 2002; Suzuki and Fox-Kemper 2016)

$$\begin{aligned} \frac{\partial u}{\partial t} = & -\frac{\partial uu}{\partial x} - \frac{\partial uv}{\partial y} - \frac{\partial uw}{\partial z} - \frac{\partial \pi}{\partial x} - f_{hy}w + f(v + v^{\text{St}}) \\ & + v^{\text{St}}\omega_z - \frac{\partial \tau_{1j}}{\partial x_j}, \end{aligned} \quad (6)$$

$$\begin{aligned} \frac{\partial v}{\partial t} = & -\frac{\partial vu}{\partial x} - \frac{\partial vv}{\partial y} - \frac{\partial vw}{\partial z} - \frac{\partial \pi}{\partial y} + f_{hx}w - f(u + u^{\text{St}}) \\ & - u^{\text{St}}\omega_z - \frac{\partial \tau_{2j}}{\partial x_j}, \quad \text{and} \end{aligned} \quad (7)$$

$$\begin{aligned} \frac{\partial w}{\partial t} = & -\frac{\partial wu}{\partial x} - \frac{\partial wv}{\partial y} - \frac{\partial ww}{\partial z} - \frac{\partial \pi}{\partial z} - \frac{\rho}{\hat{\rho}_0}g - f_{hx}(v + v^{\text{St}}) \\ & + f_{hy}(u + u^{\text{St}}) + u^{\text{St}}\omega_y - v^{\text{St}}\omega_x - \frac{\partial \tau_{3j}}{\partial x_j}, \end{aligned} \quad (8)$$

where filtered (resolved) variables are denoted by lower cases. Parameter π is the generalized pressure field (e.g., Sullivan et al. 2007): $\pi = p/\hat{\rho}_0 + 2/3e + 1/2[(u_j + u_j^{\text{St}})^2 - u_j u_j]$ with resolved pressure p , reference density $\hat{\rho}_0$, resolved velocity $u_j = (u, v, w)$, and Stokes drift $u_j^{\text{St}} = (u^{\text{St}}, v^{\text{St}}, 0)$. Term e is the subgrid-scale (SGS) TKE calculated following Sullivan et al. (2007); the SGS

viscosity is calculated without the near-surface correction by Sullivan et al. (1994); $(\omega_x, \omega_y, \omega_z) = \nabla \times (u, v, w)$ are the resolved vorticities; τ_{ij} are the SGS fluxes as evaluated in the LES parameterization model; f is the Coriolis parameter; and ρ is the water density. An upwind scheme is used for scalars in the vertical advection.

The model has been used to study the oceanic surface boundary layer turbulence driven by a variety of surface and lateral boundary conditions (e.g., Sullivan and McWilliams 2010; Kukulka et al. 2011; McWilliams et al. 2012; Sullivan et al. 2012; Van Roekel et al. 2012; Hamlington et al. 2014; McWilliams et al. 2014). It has also been successfully applied to the study of tracers including marine debris (Brunner et al. 2015; Kukulka and Brunner 2015; Kukulka et al. 2016), gas bubbles (Liang et al. 2011, 2012, 2017), and other tracers (Smith et al. 2016).

b. Model configuration

The model is configured on a rectangular domain of $300\text{ m} \times 300\text{ m} \times 300\text{ m}$ with $200 \times 200 \times 128$ grids. The horizontal grids are evenly spaced ($dx = dy = 1.5\text{ m}$) and the vertical grids are stretched with the finest resolution ($dz = 0.5\text{ m}$) at the surface, and sensitivity tests confirm that further decreases in grid spacing and grid anisotropy factor do not qualitatively change the result (not shown). Four groups of simulations, differing in surface meteorological conditions, are summarized in Table 1. Case *E* is experiments driven solely by wind; Case *L* is experiments driven by both wind and wave in equilibrium with wind; Case *S* is experiments driven by wind and wind-following swell; and Case *M* is experiments driven by wind and wind-opposing swell. These selected swell conditions are extreme; the effect of f_h under a realistic weaker swell can be inferred from the combination of all four cases. Superscript *s* denotes experiments with stratification, and subscript *h* denotes experiments with both horizontal and vertical components of planetary rotation. Eight wind directions with constant wind speed (from northward wind clockwise to northwestward wind, with 45° interval) are included. The time step is dynamically determined by the Courant–Friedrichs–Lewy (CFL) condition (Sullivan et al. 1996). Each simulation was run for approximately three inertial periods following a spinup simulation for about one inertial period. In each experiment, all the statistics are averaged over two inertial periods after turbulence becomes fully developed, and a sensitivity test shows that a longer averaging period will not affect the statistics. In this paper, we choose 5 m s^{-1} as the wind speed at 10 m above the surface. The corresponding wind stress τ is 0.040 N m^{-2} , and the waterside friction velocity u_* is 0.0063 m s^{-1} , using the drag law by Liu et al. (1979). For the case with

TABLE 1. Model configuration for different simulations.

Wave forcing	Case	Latitude	Planetary rotation	θ	La	Stratification
No wave effects (Ekman turbulence)	E	15°N, 45°N, 15°S, 45°S	f	0°	∞	Neutral
	E^s	15°N	f	0°	∞	Stable
	E_h	15°N, 45°N, 15°S, 45°S	f_h and f	0°–360°; 45° interval	∞	Neutral
	E_h^s	15°N	f_h and f	0°–360°; 45° interval	∞	Stable
Wind-following wave (wave-driven turbulence)	L	15°N	f	0°	0.35	Neutral
	L^s	15°N	f	0°	0.35	Stable
	L_h	15°N	f_h and f	0°–360°; 45° interval	0.35	Neutral
	L_h^s	15°N	f_h and f	0°–360°; 45° interval	0.35	Stable
Wind-following swell	S	15°N	f	0°	0.25	Neutral
	S_h	15°N	f_h and f	0°–360°; 45° interval	0.25	Neutral
Wind-opposing swell (shear-driven turbulence)	M	15°N	f	0°	—	Neutral
	M^s	15°N	f	0°	—	Stable
	M_h	15°N	f_h and f	0°–360°; 45° interval	—	Neutral
	M_h^s	15°N	f_h and f	0°–360°; 45° interval	—	Stable

stratification, the initial mixed layer is 40 m deep. Below the mixed layer, a stable stratification of $d\Theta/dz = 0.05 \text{ K m}^{-1}$, corresponding to a Brunt–Väisälä frequency of 0.0099 s^{-1} , is prescribed. The radiation boundary condition is applied at the lower boundary of the computational domain (Klemp and Durran 1983). We also choose 15°N as the latitude for controlled experiments ($f = 3.76 \times 10^{-5} \text{ s}^{-1}$). Additional experiments at 15°S and 45°N were also carried out to investigate how the f_h effect changes with latitude and hemisphere. The turbulent Langmuir number [$\text{La} = (u_*/u_s)^{1/2}$, where u_s is the Stokes drift at the center of the first vertical grid cell] is 0.35 for the wave-driven Langmuir case, and the Stokes drift $u^{\text{St}}(z)$ follows the formula by McWilliams and Restrepo (1999) and Sullivan et al. (2007): $u^{\text{St}}(z) = 2/g \int_0^\infty F(\tilde{\sigma}) \tilde{\sigma}^3 \exp(2\tilde{\sigma}^2 z/g) d\tilde{\sigma}$, where g is the gravitational acceleration, $\tilde{\sigma}$ is the radial frequency, and F is the wave spectrum proposed by Donelan et al. (1985) and Alves et al. (2003).

4. Model results

a. Unstratified turbulent Ekman layer

In this section, we first revisit the turbulent Ekman layer by Zikanov et al. (2003) and expand the analysis of the role of f_h in the turbulent Ekman layer. Our discussion is based on a series of numerical experiments at 15°N in the absence of stratification and nonbreaking surface gravity waves (experiments E_h and E). For the convenience of subsequent discussion, we use the following notation: for a given variable X , $\langle X \rangle_L$ denotes the horizontal average over the boundary (mixed) layer (layer-averaged variable); that is, $\langle X \rangle_L = 1/h_B \int_{h_B}^0 \langle X \rangle dz$, where h_B is the boundary (mixed) layer depth, X_{VI} denotes vertically integrated X over the boundary (mixed) layer (i.e., $X_{\text{VI}} = \int_{h_B}^0 \langle X \rangle dz$), and $\langle X \rangle_T$ denotes the ensemble average.

An instantaneous snapshot of vertical velocity fluctuation $w(x, y)$ can be used to illustrate the f_h effect on the turbulent flow structure. Eddies are larger and more coherent horizontally when the wind blows southward to westward ($\theta = [180^\circ, 270^\circ]$; i.e., from southward wind to westward wind in a clockwise sense) than when $f_h = 0$, while eddies are smaller and more intermittent in horizontal dimensions when the wind blows northward to eastward ($\theta = [0^\circ, 90^\circ]$; Fig. 2). To quantify this, we use the velocity correlation function (Davidson 2015)

$$\text{CF}(r) = \langle w(x, y, z) w(x + r_x, y + r_y, z) \rangle,$$

with $r = \sqrt{r_x^2 + r_y^2}$, then calculate the shortest length r_s where $\text{CF}(r_s) = 0.05\text{CF}(r=0)$. Eddies that are larger and more coherent horizontally will have larger r_s , and vice versa (see Fig. 3g). The instantaneous w patterns of different wind directions are not noticeably different close to the surface (not shown) and are evidently different in the middle of the boundary layer. This is due to the role of f_h in rotating the horizontal velocity into vertical velocity. Although the equilibrium value of vertical velocity variance is not directly determined by the sign of the terms with f_h (see section 2), the enhancement or reduction of vertical velocity variance $\langle w^2 \rangle$ is associated with the signs of f_{hx} , f_{hy} , $\langle u'w \rangle$, and $\langle v'w \rangle$ [see Eq. (3)]. Vertical velocity variance increases when both $f_{hy}\langle u'w \rangle$ and $-f_{hx}\langle v'w \rangle$ are positive. This occurs, for instance, when the wind is southwestward ($\theta = 225^\circ$) in the Northern Hemisphere, when both f_{hx} and f_{hy} are negative, $\langle u'w \rangle$ is negative, and $\langle v'w \rangle$ is positive. Comparisons of instantaneous snapshots for w and r_s show that the scale of eddies and vertical TKE are larger than when $f_h = 0$. In this regime, vertical turbulent mixing is strengthened. In contrast, vertical velocity variance decreases when both $f_{hy}\langle u'w \rangle$ and $-f_{hx}\langle v'w \rangle$ are negative.

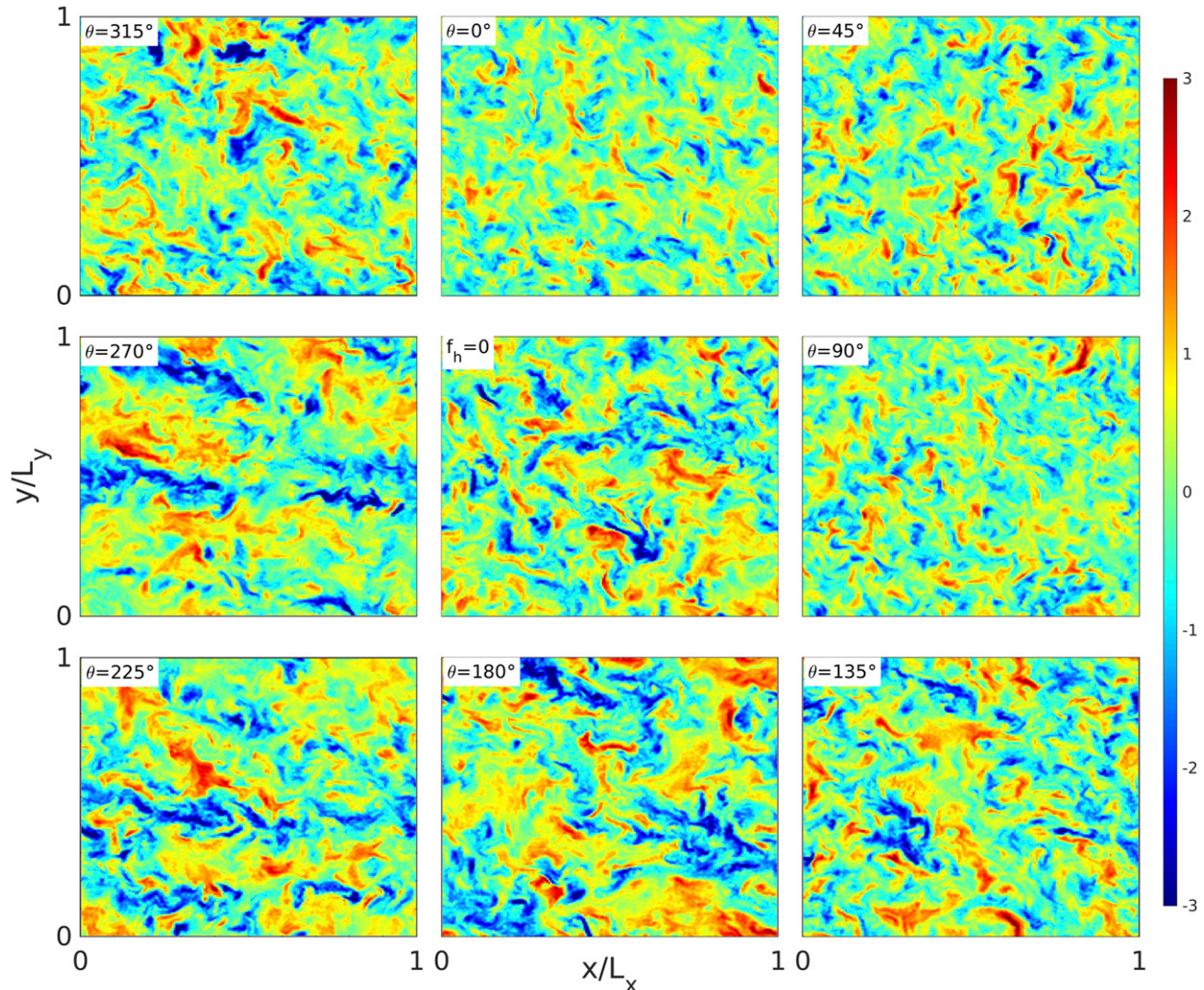


FIG. 2. The instantaneous snapshot of $w(x, y)$ at $z = -30$ m for unstratified Ekman turbulence at 15°N , normalized by u_* . Here, L_x and L_y are the lengths of computational domain along downwind and crosswind directions, respectively. The center panel is the case when $f_h = 0$, and around the edge are the cases with $f_h \neq 0$ located in their compass positions.

This occurs, for example, when the wind is northeastward ($\theta = 45^\circ$) in the Northern Hemisphere, when both f_{hx} and f_{hy} are positive, $\langle u'w \rangle$ is negative, and $\langle v'w \rangle$ is positive. Comparisons of instantaneous snapshots for w and r_s show that the scale of eddies and vertical TKE are smaller than when $f_h = 0$. Vertical turbulent mixing is also weakened in this regime. The enhanced (weakened) vertical turbulent mixing also affects the vertical extent of the boundary layer. For instance, 60 m is inside the boundary layer for a southward wind, while it is outside the boundary layer for a northward wind.

Under the influence of f , the mean surface currents (U_0, V_0) are deflected to the right of the wind and rotate clockwise with depth in the Northern Hemisphere (Ekman 1905), and the velocity spiral is independent of wind direction. In the presence of f_h , both the deflection

and the magnitude of the mean horizontal current vary with wind direction (Fig. 3a): when the wind blows northward to southeastward ($\theta = [0^\circ, 135^\circ]$), the mean surface current is deflected more to the right of the wind, as indicated by a larger angle between wind stress and surface current. When the wind blows southward to northwestward ($\theta = [180^\circ, 315^\circ]$), the deflection is less (cf. Fig. 7 in Zikanov et al. 2003).¹ For instance, the mean surface current is 31.1° to the right of the wind when the wind blows northward ($\theta = 0^\circ$), while it is only 18.7° to the right when the wind blows southward ($\theta = 180^\circ$).

¹ As McWilliams and Huckle (2006) suggested, the angle γ used in Zikanov et al. (2003) is interpreted as the angle from the wind stress direction to the north direction measured in a counterclockwise sense.

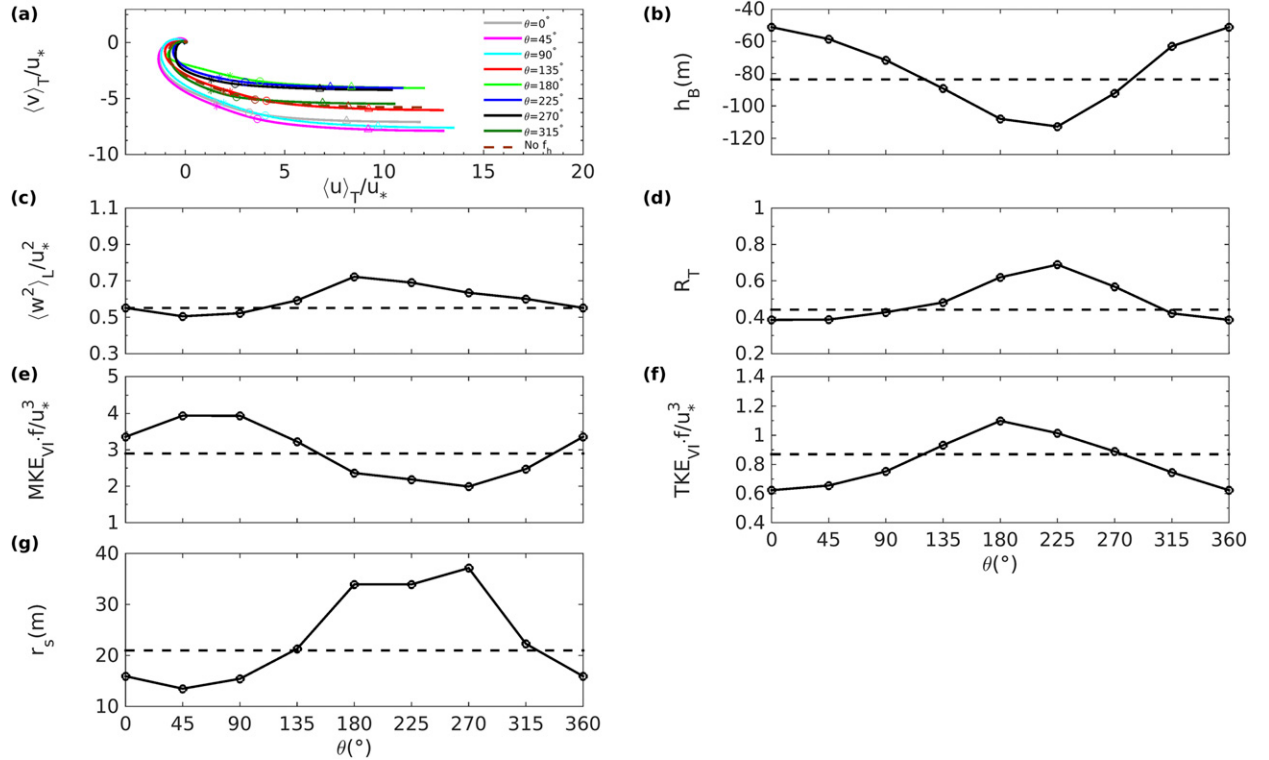


FIG. 3. Effects of wind direction θ on unstratified Ekman turbulence at 15°N : (a) mean velocity hodographs with symbols indicating different depths: -1 (triangle), -5 (circle), and -10 m (asterisk); the line color convention is $\theta = 0^\circ$ (gray), $\theta = 45^\circ$ (magenta), $\theta = 90^\circ$ (light blue), $\theta = 135^\circ$ (red), $\theta = 180^\circ$ (light green), $\theta = 225^\circ$ (dark blue), $\theta = 270^\circ$ (black), $\theta = 315^\circ$ (dark green), and $f_h = 0$ (brown). (b) Boundary layer depth h_B ; (c) layer-averaged variance of vertical velocity $\langle w^2 \rangle_L$, normalized by u_*^2 ; (d) the ratio of vertical component to horizontal component of TKE $R_T = 2\langle w^2 \rangle_L / \langle u^2 + v^2 \rangle_L$. (e) Vertically integrated MKE over the boundary layer $MKE_{VI} = 1/2 \int_{h_B}^0 (\langle u^2 \rangle + \langle v^2 \rangle) dz$, normalized by u_*^3/f ; (f) vertically integrated total (resolved + SGS) TKE over the boundary layer $TKE_{VI} = \int_{h_B}^0 [1/2(\langle u^2 \rangle + \langle v^2 \rangle + \langle w^2 \rangle) + \langle e \rangle] dz$, normalized by u_*^3/f . (g) Parameter r_s (m) calculated from structure function $CF(r)$ at $z = -30$ m. All solid lines indicate results when $f_h \neq 0$, and dashed lines indicate when $f_h = 0$.

The change in mean horizontal velocity by f_h is due to the modulation of the vertical momentum fluxes ($\langle u'w \rangle$, $\langle v'w \rangle$) by f_h (Zikanov et al. 2003). When the wind blows northward to southeastward ($\theta = [0^\circ, 135^\circ]$), the near-surface gradient for $\langle u'w \rangle$ increases due to f_h , resulting in a more negative V_0 . When the wind blows in the opposite directions ($\theta = [180^\circ, 315^\circ]$), the near-surface gradient for $\langle u'w \rangle$ decreases due to f_h , resulting in a less negative V_0 . The change in U_0 is less dramatic than the change in V_0 because of the smaller change in the near-surface $\langle v'w \rangle$ gradient than in the near-surface $\langle u'w \rangle$ gradient. The mean surface horizontal current (U_0 and V_0) is particularly important in determining the transport and dispersion of many pollutants, such as spilled oil and marine debris, that are positively buoyant and are trapped near the surface. It is also important to determine the wind work to the ocean. The maximum time rate of wind work ($P_w = \rho_w u_*^2 U_0$, where ρ_w is water density) when the wind blows eastward ($\theta = 90^\circ$) is 30% larger than the minimum when the wind blows westward ($\theta = 270^\circ$) at 15°N (not

shown). The magnitude of the mean current decays faster when the wind blows northward to eastward than the opposite wind directions (Fig. 3a). The effect of f_h on the mean horizontal Ekman current in the absence of stratification and surface gravity waves is consistent with the previous studies (Coleman et al. 1990; Zikanov et al. 2003; McWilliams and Huckle 2006).

Boundary layer depth h_B is also significantly modified by f_h (Fig. 3b). Here, the boundary layer depth h_B is defined as the depth at which the horizontally and time-averaged momentum flux is 10% of the surface momentum flux u_*^2 . Sensitivity tests indicate that a smaller criterion (less than 10%) of surface momentum flux used in the definition of h_B influences the magnitude of h_B , but does not change the dependence of h_B on wind direction (not shown). Compared with the $f_h = 0$ case (dashed line), the boundary layer is deeper for southeastward to westward winds ($135^\circ \leq \theta \leq 270^\circ$) and is shallower for other directions. The maximum h_B is twice as large as the minimum h_B .

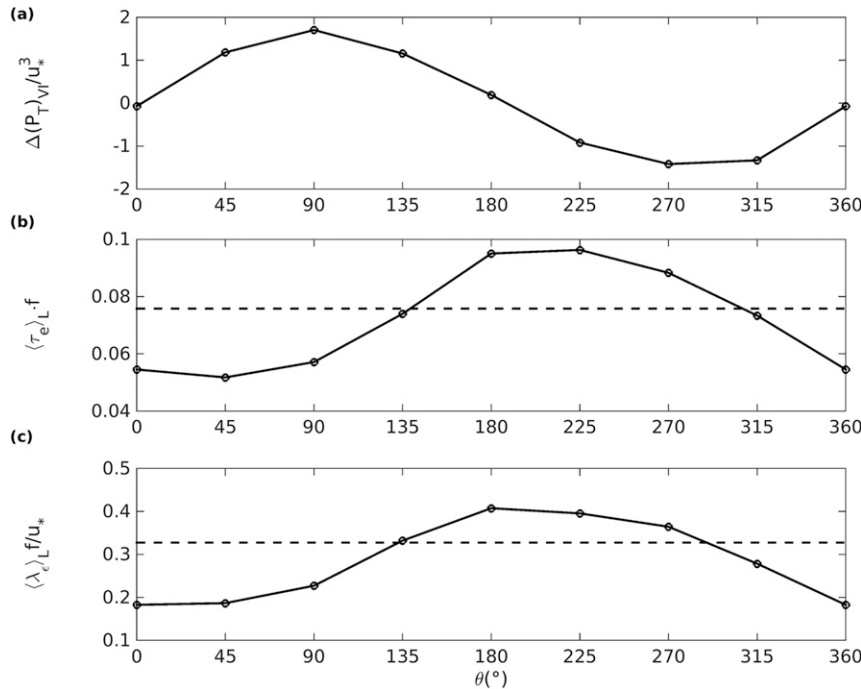


FIG. 4. Effects of wind direction θ on unstratified Ekman turbulence at 15°N: (a) the difference of vertically integrated total TKE production $\Delta(P_T)_{VI}$ over the boundary layer between $f_h \neq 0$ and $f_h = 0$, normalized by u_*^3 ; (b) layer-averaged eddy turnover time $\langle\tau_e\rangle_L$, normalized by $1/f$; (c) layer-averaged dissipation scale $\langle\lambda_e\rangle_L$, normalized by u_*/f . The solid line denotes $f_h \neq 0$ cases, and the dashed line denotes the $f_h = 0$ case.

The depth of the equilibrium OSBL is a function of the characteristic length scale of the turbulent flow. The commonly used length scales to characterize boundary layers are the Ekman depth u_*/f (Rossby and Montgomery 1935) under the sole influence of wind stress and the Obukhov length (Monin and Obukhov 1954) with the combined effect of wind stress and a destabilizing buoyancy flux. However, neither length scale includes the wind direction dependence of boundary layer depth under the influence of f_h .

We find that the wind direction dependence of h_B is the same as the wind direction dependence of the layer-averaged vertical velocity variance $\langle w^2 \rangle_L$ (Fig. 3c), indicating the variation of h_B is controlled by the vertical TKE. The $\langle w^2 \rangle_L$ is the average taken over the boundary layer, ranging from 0.51 to 0.72. The turbulent kinetic energy is redistributed from the vertical to horizontal component when both f_{hx} and f_{hy} are positive ($0^\circ < \theta < 90^\circ$) and from the horizontal to vertical direction when both f_{hx} and f_{hy} are negative ($180^\circ < \theta < 270^\circ$). The redistribution of TKE can be inferred from the ratio between vertical and horizontal variances ($R_T = 2\langle w^2 \rangle_L / (\langle u^2 \rangle_L + \langle v^2 \rangle_L)$; Fig. 3d). The ratio R_T is larger than the $f_h = 0$ case when $180^\circ < \theta < 270^\circ$ and smaller than the $f_h = 0$ case when $0^\circ < \theta < 90^\circ$. This is associated with larger $\langle w^2 \rangle_L$ for

southward to westward winds as well. In this case, turbulence with a larger $\langle w^2 \rangle_L$ can penetrate deeper, which induces a deeper h_B .

The vertically integrated mean kinetic energy (MKE) over the boundary layer [$MKE_{VI} = 1/2 \int_{h_B}^0 (\langle u^2 \rangle + \langle v^2 \rangle) dz$] is shown as a function of wind direction θ in Fig. 3e. It is clear that MKE_{VI} increases for cases $0^\circ < \theta < 90^\circ$, compared with the $f_h = 0$ case, and decreases for cases $180^\circ < \theta < 270^\circ$. The variation of MKE_{VI} is affected by both the variation of momentum flux that can affect the shear production of turbulence and the variation of wind work at the water surface.

The vertically integrated turbulent kinetic energy over the boundary layer [$TKE_{VI} = \int_{h_B}^0 [1/2(\langle u^2 \rangle + \langle v^2 \rangle + \langle w^2 \rangle) + \langle e \rangle] dz$], normalized by u_*^2 , is shown in Fig. 3f. In particular, TKE_{VI} is smaller than the $f_h = 0$ case for $0^\circ < \theta < 90^\circ$, which is consistent with Zikanov et al. (2003, their Fig. 9a). Note that the f plane used in Zikanov et al. (2003) is chosen at 90°N, which has a stronger suppression on turbulence due to a larger f .

The variability in r_s to wind direction at the vertical depth ($z = -30$ m), where the instantaneous snapshot of $w(x, y)$ is taken, is shown in Fig. 3g. The distance r_s is smaller when the wind blows northward to eastward than the $f_h = 0$ case. In contrast, r_s is larger when the wind

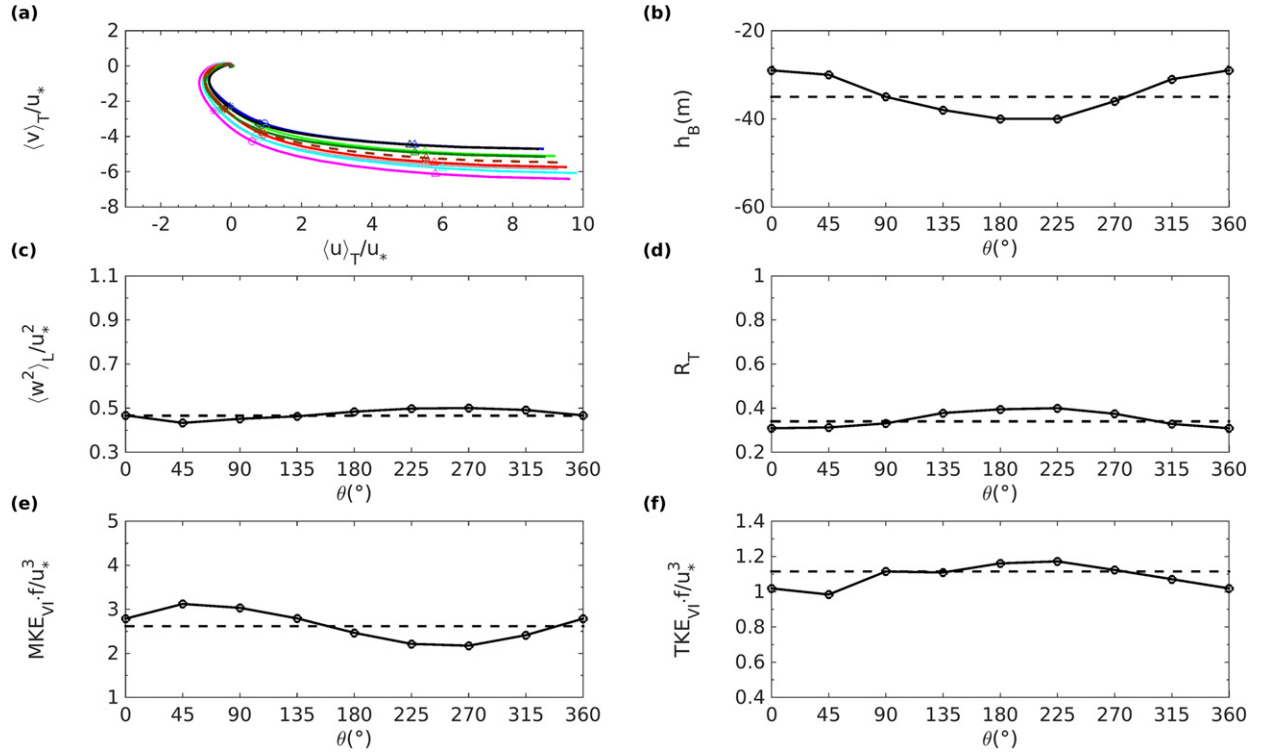


FIG. 5. As in Fig. 3, but at 45°N.

blows southward to westward than the $f_h = 0$ case. This is consistent with the instantaneous snapshot (Fig. 2).

Contrary to the conjecture by Zikanov et al. (2003) that the difference in TKE production ($-\langle u'_j w \rangle \partial \langle u_j \rangle / \partial z$) among wind directions governs the difference in the magnitudes of TKE, the wind direction dependence of total TKE production (Fig. 4a) is different from that of TKE_{VI} (Fig. 3f). For instance, the total production of TKE is the largest (smallest) for eastward (westward) wind (Fig. 4a). The production of TKE is maximum at the surface where the mean current shear ($\partial \langle u \rangle / \partial z$, $\partial \langle v \rangle / \partial z$) is the largest. It therefore has the same wind direction dependence as the surface mean current (Fig. 3a). Although f_h can influence the profiles of momentum flux ($\langle u'w \rangle$, $\langle v'w \rangle$), its effect is larger in the middle of the boundary layer and is negligible close to the surface where shear is the largest (cf. Fig. 8 in Zikanov et al. 2003).

The wind direction dependence of layer-averaged eddy turnover time $\langle \tau_e \rangle_L$ (the ratio of total TKE to dissipation; Fig. 4b) dominates the wind direction dependence of TKE_{VI} . It is also larger than the $f_h = 0$ case for cases $180^\circ < \theta < 270^\circ$ and smaller than the $f_h = 0$ case for cases $0^\circ < \theta < 90^\circ$. The largest eddy turnover time is approximately twice as large as the smallest value in unstratified Ekman turbulence.

The wind direction dependence of eddy turnover time can also be interpreted by examining the dissipation length scale λ_ε , defined as

$$\lambda_\varepsilon = \frac{\mathcal{E}^{3/2}}{\varepsilon}, \quad (9)$$

where \mathcal{E} is the turbulent kinetic energy, and ε is the dissipation rate (Tennekes and Lumley 1972; Grant and Belcher 2009). The averaged dissipation length scale over the boundary layer is shown in Fig. 4c. Larger $\langle \lambda_\varepsilon \rangle_L$ corresponds to larger $\langle \tau_e \rangle_L$, meaning that larger eddies with more energy spend more time dissipating energy into smaller eddies.

b. Modification of the f_h effect due to latitude and hemisphere

Compared with 15°N, the magnitude of the mean surface current (U_0 , V_0) decreases due to increasing f at 45°N (Fig. 5a). The variation of the angle between wind stress and surface current also decreases as latitude increases: the difference between the largest and smallest angle decreases from 12.6° at 15°N to 5.7° at 45°N. The boundary layer depth increases as θ increases when $0^\circ < \theta < 180^\circ$, which qualitatively agrees with the result that growth rate for the most unstable mode increases as the Ekman-layer surface-current direction increases

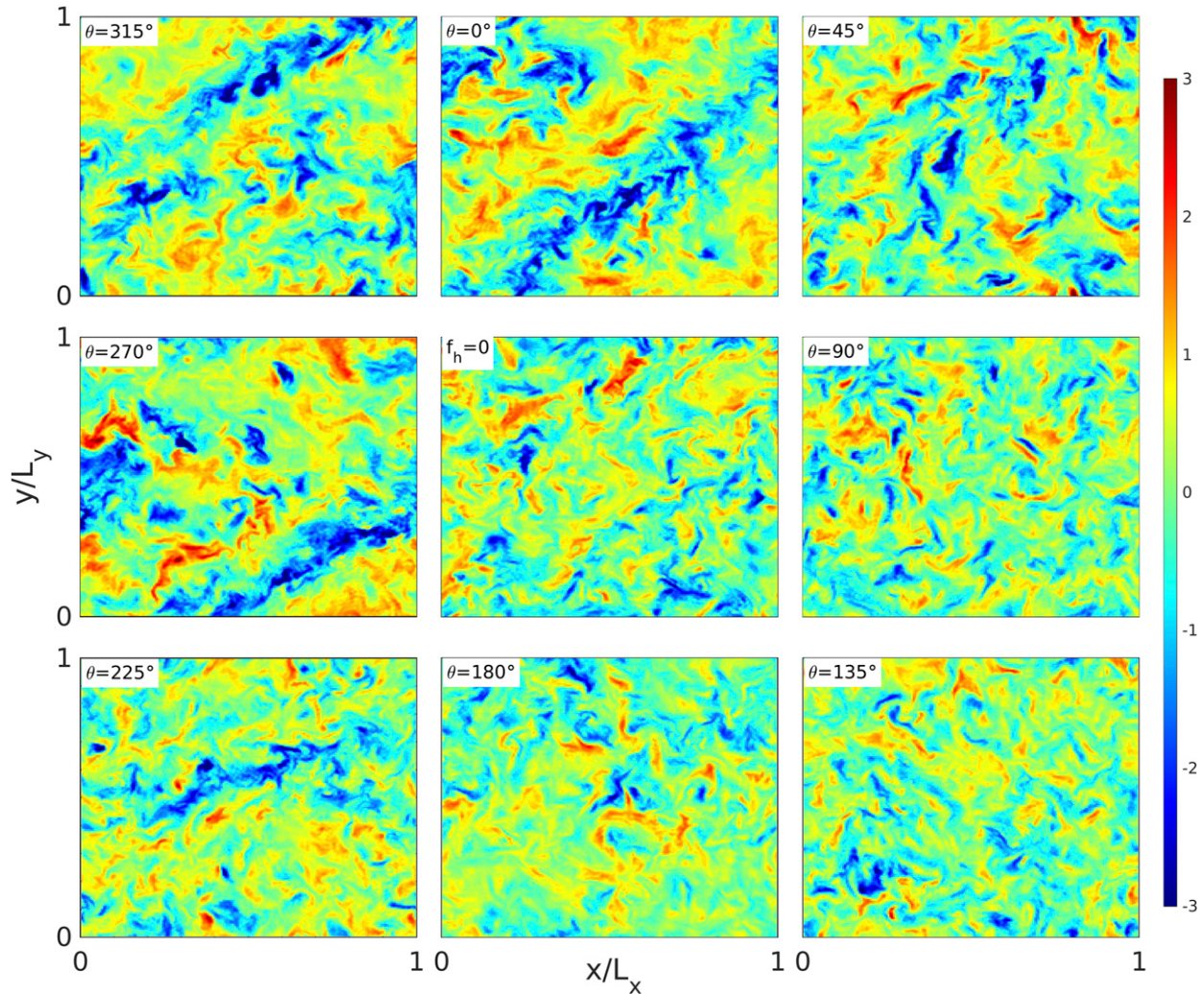


FIG. 6. As in Fig. 2, but for $z = -40$ m for unstratified Ekman turbulence at 15°S .

based on a series of linear instability analyses (cf. Fig. 19 in Leibovich and Lele 1985). Moreover, in the same hemisphere, the variabilities in h_B , $\langle w^2 \rangle_L$, R_T , MKE_{VI}, and TKE_{VI}, defined as the ratio of the difference between the maximum and minimum values to the minimum value, decrease from 120%, 43%, 79%, 98%, and 76% at 15°N (Figs. 3b–f) to 38%, 16%, 30%, 44%, and 19% at 45°N (Figs. 5b–f), respectively.

Although f_h is the same at the same latitude in opposite hemispheres, the dependence of turbulence on wind direction is different because of the reversed vertical rotation in opposite hemispheres. An instantaneous snapshot of vertical velocity fluctuation $w(x, y)$ at 15°S is used to show the major difference in instantaneous flow structure in the middle of the water column, where the f_h effect is obvious (Fig. 6). Turbulent flow is more coherent and is of larger horizontal scale when the wind

blows westward to northward ($\theta = [270^\circ, 360^\circ]$; i.e., from a westward wind to a northward wind in a clockwise sense) than when $f_h = 0$, while turbulence is more intermittent and is of smaller spatial space when the wind blows eastward to southward ($\theta = [90^\circ, 180^\circ]$).

Under the influence of negative f , mean surface current (U_0, V_0) is deflected to the left of the wind and rotates counterclockwise with depth in the Southern Hemisphere (Ekman 1905). The mean horizontal velocity has a different wind direction dependence at 15°S (Fig. 7a) than at 15°N : the mean surface current is deflected more to the left of the wind than without the influence of f_h , indicated by a larger angle between wind stress and surface current when the wind blows eastward to southward ($\theta = [90^\circ, 180^\circ]$), and is deflected less when the wind blows westward to northward ($\theta = [270^\circ, 360^\circ]$).

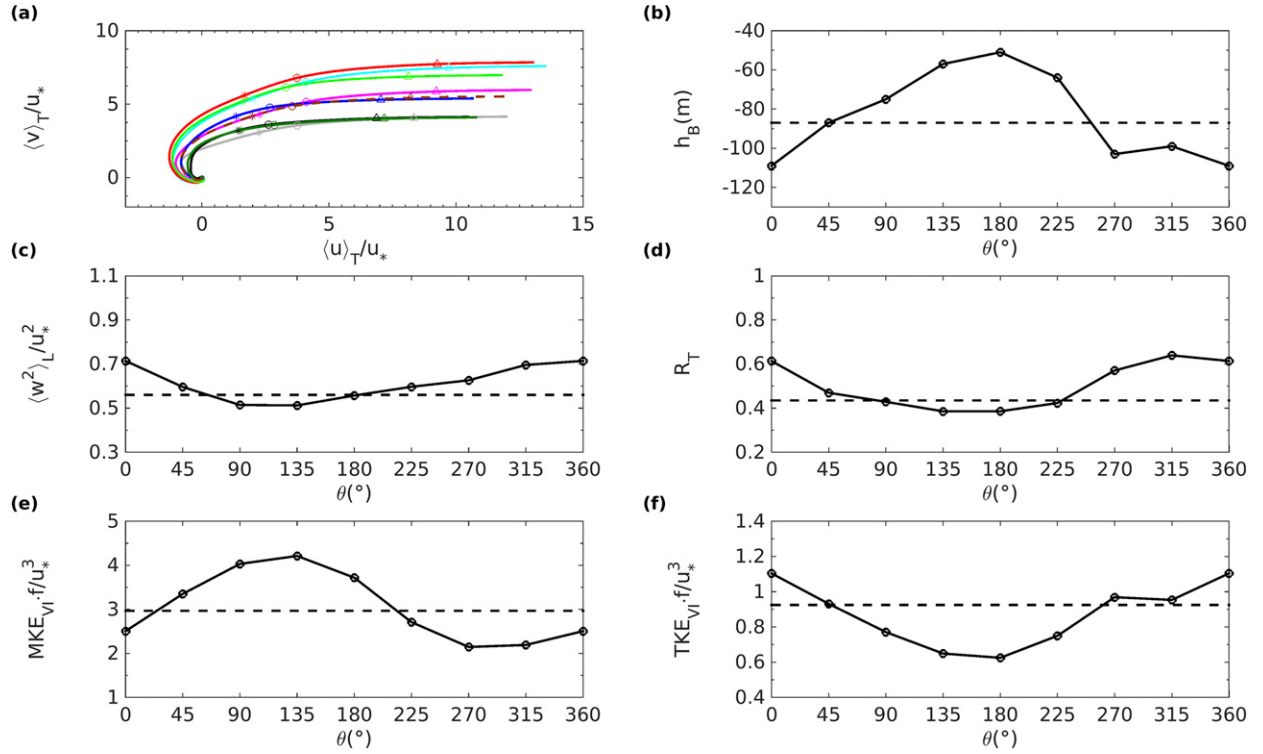


FIG. 7. As in Fig. 3, but at 15°S.

Different from 15°N, h_B is larger for westward to northward wind ($270^\circ \leq \theta \leq 360^\circ$) than when $f_h = 0$ at 15°S (Fig. 7b). In particular, the boundary layer is the shallowest for a southward wind ($\theta = 180^\circ$) and the deepest for a northward wind ($\theta = 0^\circ$). Similar to 15°N, the maximum h_B is twice as large as the minimum h_B at 15°S.

Similar to the variation in h_B , the values of $\langle w^2 \rangle_L$ (Fig. 7c), R_T (Fig. 7d), and TKE_{VI} (Fig. 7f) are larger than the $f_h = 0$ case when the wind blows westward to northward and smaller than the $f_h = 0$ case when the wind blows eastward to southward. It is obvious that MKE_{VI} increases for cases $90^\circ < \theta < 180^\circ$, compared with the $f_h = 0$ case, and decreases for cases $270^\circ < \theta < 360^\circ$ (Fig. 7e).

The magnitude of the mean surface current decreases at 45°S (Fig. 8a) due to larger magnitude of f , compared to at 15°S. The variabilities in h_B , $\langle w^2 \rangle_L$, R_T , MKE_{VI}, and TKE_{VI} to wind direction also reduce as latitude increases in the Southern Hemisphere from 113%, 39%, 66%, 96%, and 77% at 15°S (Figs. 7b–f) to 52%, 14%, 39%, 44%, and 26% at 45°S (Figs. 8b–f), respectively. The hemisphere dependence of the f_h effect is associated with the signs of f_{hx} , f_{hy} , $\langle u'w \rangle$, and $\langle v'w \rangle$ as well: turbulence is enhanced when the wind has a westward and southward component ($180^\circ < \theta < 270^\circ$) in the Northern

Hemisphere and strengthened when the wind has a westward and northward wind ($270^\circ < \theta < 360^\circ$) in the Southern Hemisphere, both of which have positive values for both $f_{hy}\langle u'w \rangle$ and $-f_{hx}\langle v'w \rangle$ (within the boundary layer, $\langle u'w \rangle$ is negative in both hemispheres, and $\langle v'w \rangle$ is positive in the Northern Hemisphere and negative in the Southern Hemisphere). Turbulence is reduced when the wind has an eastward and northward component ($0^\circ < \theta < 90^\circ$) in the Northern Hemisphere and is weakened when the wind has an eastward and southward component ($90^\circ < \theta < 180^\circ$) in the Southern Hemisphere, both of which have negative values for both $f_{hy}\langle u'w \rangle$ and $-f_{hx}\langle v'w \rangle$.

c. Modification of the f_h effect due to stratification

The mixed layer is generally shallow and is capped by stable stratification at low to midlatitudes. The modification of the f_h effect on Ekman turbulence by stable stratification is studied with experiments E_h^s and E^s (Table 1). Similar to unstratified Ekman turbulence (Fig. 2), the horizontal scale of convergence regions for a southwestward wind is larger than for a northeastward wind inside the boundary layer (not shown), although the difference is less obvious than in the unstratified Ekman turbulence. Similar to the unstratified Ekman turbulence, the f_h effect in the vertical velocity fluctuation is

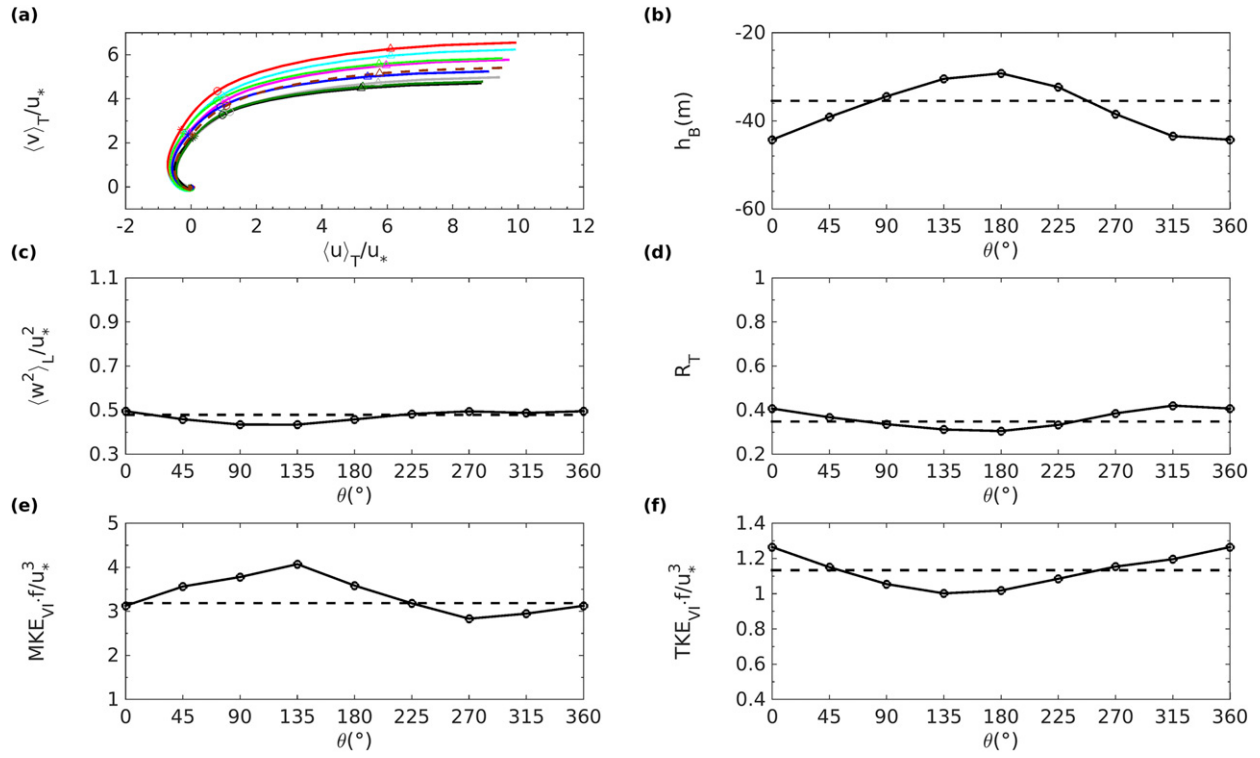


FIG. 8. As in Fig. 3, but at 45°S.

negligible at the surface in stratified Ekman turbulence. In the lower part of the boundary layer, the wind direction dependence of flow structure is insignificant because of the reduced $\langle w^2 \rangle$.

Compared with unstratified Ekman cases (Cases E_h and E), Fig. 9a shows that the variability in the mean flow to wind direction is reduced by stratification. The stratification reduces the difference in the angle β between surface mean current and wind stress significantly (Fig. 9b). The difference in β between maximum and minimum reduces from 12.6° in unstratified Ekman cases to 3.3° in stratified Ekman cases. The variability in mean surface current is similar with and without stratification: the largest mean surface speed for an eastward wind ($\theta = 90^\circ$) is approximately 35% larger than the smallest mean surface speed for a westward wind ($\theta = 270^\circ$).

Stratification reduces the variability in vertical velocity variance $\langle w^2 \rangle_L$ (Fig. 9c): the largest $\langle w^2 \rangle_L$ is only 14% larger than the smallest. The variability in R_T reduces from 79% in unstratified Ekman turbulence (Fig. 3d) to 25% in stratified Ekman turbulence (Fig. 9d). Stratification reduces the magnitude and the variability of MKE_{VI} to wind direction (Fig. 9e). The variability in MKE_{VI} decreases from 98% in unstratified Ekman turbulence to 37% in stratified Ekman

turbulence. The variability in TKE_{VI} to wind direction in stratified Ekman turbulence (Fig. 9f) also reduces and is different from unstratified Ekman turbulence: the variability in TKE_{VI} in stratified Ekman turbulence is only 15%, which is much smaller than the variation (76%) in unstratified Ekman turbulence. The magnitude of TKE_{VI} for the $f_h = 0$ case with stratification reduces by 45%, compared with the $f_h = 0$ case without stratification. The dependence of wind work, as well as TKE dissipation rate (not shown), on the wind direction is enhanced in the presence of stratification. The largest wind work when the wind blows eastward in stratified Ekman turbulence is 36% larger than the smallest when the wind blows westward, compared with the variability (30%) in unstratified Ekman turbulence.

The average entrainment rate is calculated as $w_e = d\langle z_i \rangle / dt$ (Sullivan et al. 1998), where z_i is the depth where the potential temperature is 0.25 K smaller than the surface value. For stratified cases, the boundary layer turbulence is limited by a shallow mixed layer depth h_M , which is the temporal and horizontal average of z_i . The variability in h_M to wind direction during the relatively short integration is small (not shown). In unstratified Ekman turbulence, h_B is strongly dependent on wind direction. In the regions with a shallow mixed layer, h_B is limited by the stratification and is equal to

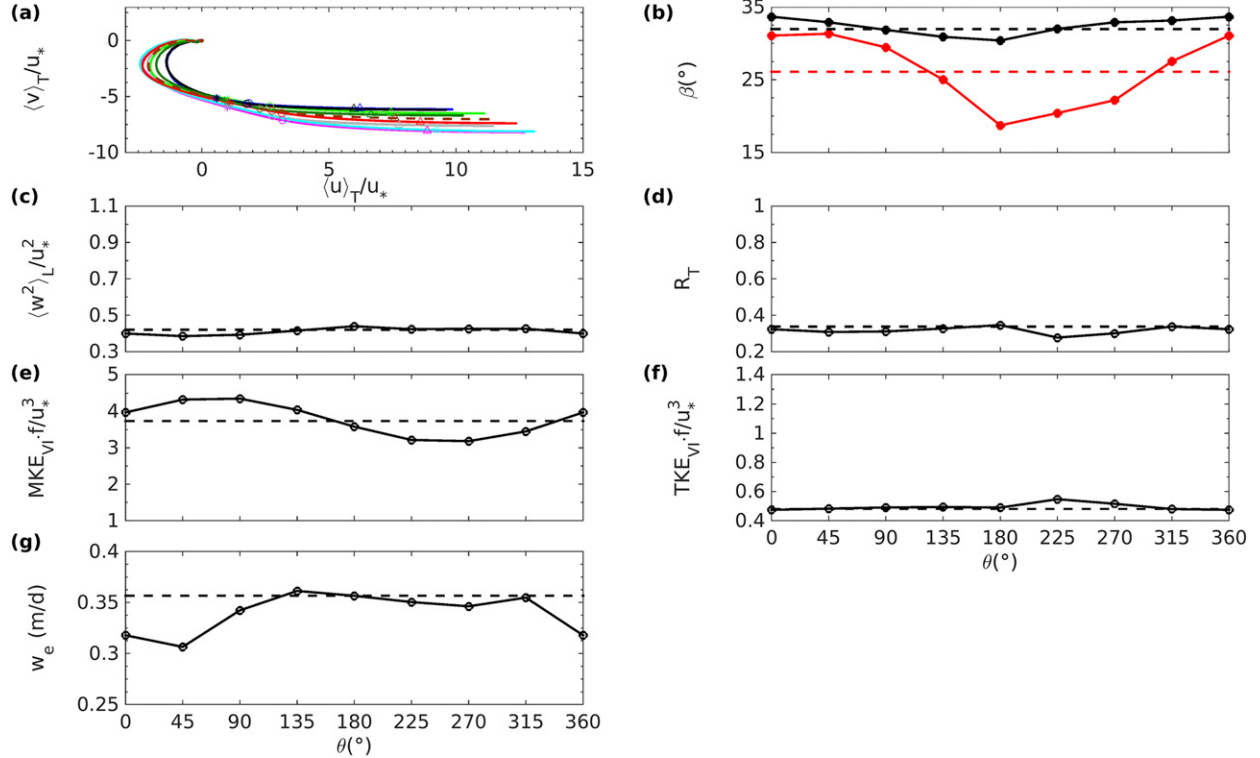


FIG. 9. Effects of wind direction θ on stratified Ekman turbulence at 15°N : (a) Lagrangian mean velocity hodographs with symbols indicating different depths: -1 (triangle), -5 (circle), and -10 m (asterisk); the line color convention is the same as in Fig. 3a. (b) Angle between surface mean current and wind stress β : unstratified Ekman turbulence with f_h (red solid), unstratified Ekman turbulence without f_h (red dashed), stratified Ekman turbulence with f_h (black solid), and stratified Ekman turbulence without f_h (black dashed). (c) Layer-averaged variance of vertical velocity $\langle w^2 \rangle_L$, normalized by u_*^2 ; (d) the ratio of vertical component to horizontal component of TKE $R_T = 2\langle w^2 \rangle_L / \langle u^2 + v^2 \rangle_L$; (e) vertically integrated MKE over the mixed layer $MKE_{VI} = 1/2 \int_{h_M}^0 (\langle u^2 \rangle + \langle v^2 \rangle) dz$, normalized by u_*^3/f . (f) Vertically integrated total (resolved + SGS) TKE over the mixed layer $TKE_{VI} = \int_{h_M}^0 [1/2(\langle u^2 \rangle + \langle v^2 \rangle + \langle w^2 \rangle)] dz$, normalized by u_*^3/f ; (g) entrainment rate w_e (m day^{-1}). All solid lines indicate results when $f_h \neq 0$, and dashed lines indicate when $f_h = 0$.

h_M (about -45 m at 15°N). The largest entrainment rate ($w_e = 0.36 \text{ m day}^{-1}$) is about 116% of the smallest ($w_e = 0.31 \text{ m day}^{-1}$; Fig. 9g). The stronger entrainment for southward to westward winds ($\theta = [180^\circ, 270^\circ]$) also explains the reduced R_T for these wind directions (Fig. 9d). When entrainment strengthens, horizontal velocity variances increase within the entrainment layer (e.g., Wang et al. 1996), leading to a lower vertical to horizontal velocity variance ratio.

The variability in velocity variance to wind direction is reduced by stratification. For stratified Ekman turbulence with $f_h = 0$, $\langle u^2 \rangle_T$ reduces by 4% at the surface, compared with the unstratified Ekman case. The maximum variance of vertical velocity fluctuation $\langle w^2 \rangle_T$ decreases by 15% due to the limitation of stratification on turbulent mixing. When f_h is considered, the difference $\langle v^2 \rangle_T - \langle w^2 \rangle_T$ reduces by 13% when the wind is northeastward and increases by 22% when the wind is southwestward at the surface. The ordering of velocity variances is $\langle w^2 \rangle_T < \langle v^2 \rangle_T < \langle u^2 \rangle_T$ above $z/|h_M| = -0.5$

for all the wind directions. Both $\langle u^2 \rangle_T - \langle w^2 \rangle_T$ and $\langle v^2 \rangle_T - \langle w^2 \rangle_T$ are positive in the whole boundary layer, while $\langle w^2 \rangle_T$ decreases rapidly below $z/|h_M| = -0.2$ (Fig. 10). The large $\langle u^2 \rangle_T$ and $\langle v^2 \rangle_T$ near the base of the mixed layer ($-0.9 < z/|h_M| < -0.8$) when the wind blows southward to westward indicate that the horizontal turbulence is strengthened when the entrainment rate is strong (e.g., Kukulka et al. 2010).

Stratification also decreases both the magnitude of eddy turnover time $\langle \tau_e \rangle_L$ and its variability to wind direction (not shown). The eddy turnover time in the $f_h = 0$ case is decreased by 41% due to stratification. When f_h is considered, the variability in eddy turnover time reduces from 86% in the unstratified Ekman turbulence to 52% in the stratified Ekman turbulence. For unstratified cases, larger $\langle \tau_e \rangle_L$ represents more time for turbulence dissipating energy and, hence, larger TKE contained in the water column, and vice versa. For stratified cases, stratification rather than eddy turnover time may have more impacts on TKE, which means

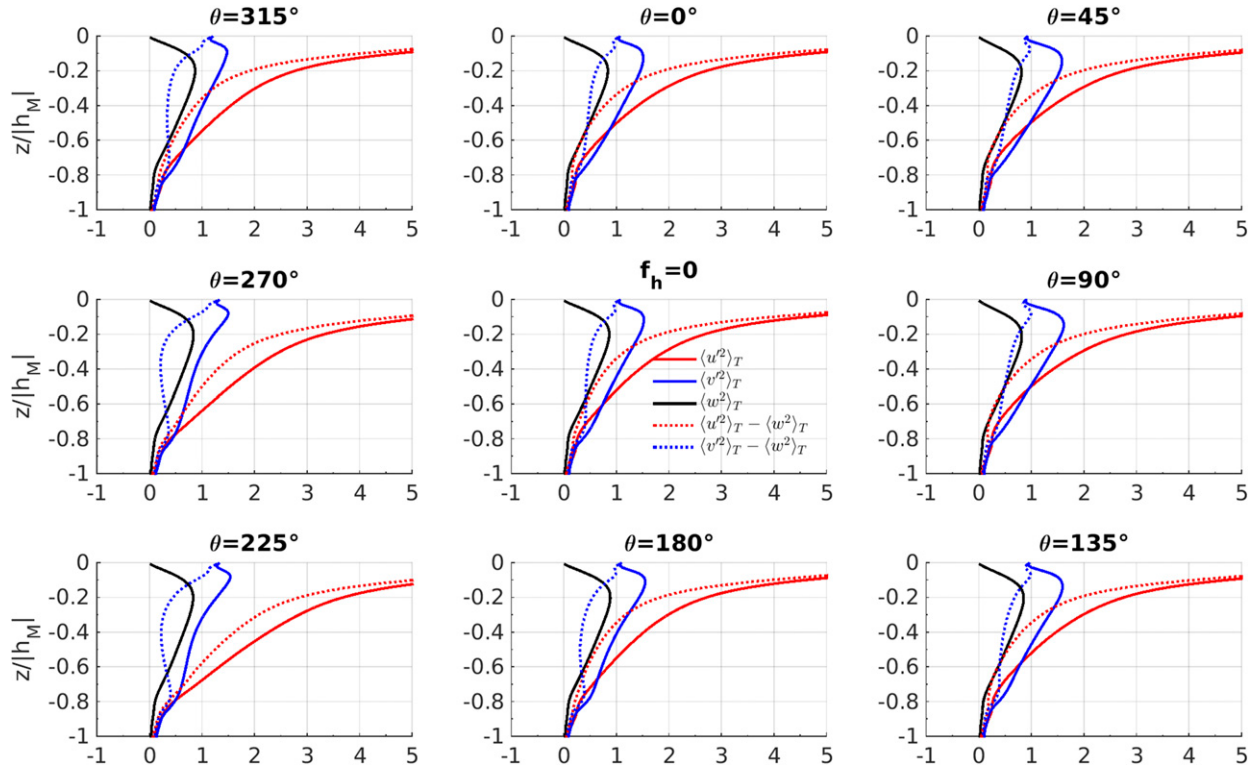


FIG. 10. Profiles of temporal- and horizontal-averaged velocity variances for stratified Ekman turbulence (15°N): $\langle u^2 \rangle_T$ (red solid), $\langle v^2 \rangle_T$ (blue solid), $\langle w^2 \rangle_T$ (black solid), $\langle u^2 \rangle_T - \langle w^2 \rangle_T$ (red dashed), and $\langle v^2 \rangle_T - \langle w^2 \rangle_T$ (blue dashed), normalized by u_*^2 . The center panel is the case when $f_h = 0$, and around the edge are the cases with $f_h \neq 0$ located in their compass positions. The vertical axis is the depth normalized by $|h_M|$.

TKE is more likely to be determined by the depth that turbulence can reach than eddy turnover time in the presence of stratification as production changes less.

d. Modification of the f_h effect by Langmuir turbulence

Nonbreaking surface gravity waves have two primary effects because of phase-averaged Stokes drift: the mean horizontal current profile is modified by Coriolis–Stokes forcing (e.g., Polton et al. 2005), and turbulent kinetic energy is enhanced through Stokes production (e.g., McWilliams et al. 1997). Also, wave–current interactions generate coherent streamwise vortices, which are signatures of Langmuir turbulence (e.g., Belcher et al. 2012). We first investigate the impact of f_h on OSBL turbulence for wind-following waves. In this regime, Stokes drift tilts vertical vorticity perturbation into horizontal vortices that align with the wind stress. Cases L_h and L represent simulations driven by wind-following, nonbreaking surface gravity waves.

For unstratified Langmuir turbulence and $f_h = 0$, the downwelling branches of the LCs are oriented roughly downwind with relatively small horizontal scales near

the surface; LCs induce streamwise streaky patterns in the vertical velocity $w(x, y)$ (not shown) and narrow forward-looking Y junctions (Farmer and Li 1995; Sullivan et al. 2007). With increasing depth, the streamwise streaks are more coherent and rotate clockwise, consistent with previous studies (e.g., McWilliams et al. 1997). In the lower part of the boundary layer (e.g., $z/|h_B| < -1/3$), the streak-like patterns are more fragmented. When f_h is considered, there are only slight differences at the surface for varying wind directions. With increasing depth, the streamwise streaks become more coherent and orient obliquely to the wind direction when the wind blows southward to westward. In contrast, the streak-like pattern becomes less organized, with mostly small scales when the wind blows northward to eastward. At the same time, the asymmetry between stronger downwelling and weaker upwelling branches of the LCs is enhanced for a southwestward wind and is reduced for a northeastward wind. The profile of conditional averaged vertical velocity (McWilliams et al. 1997; Van Roekel et al. 2012) indicates that f_h has a minimal effect on the coherent structure of Langmuir turbulence close to the surface (not shown).

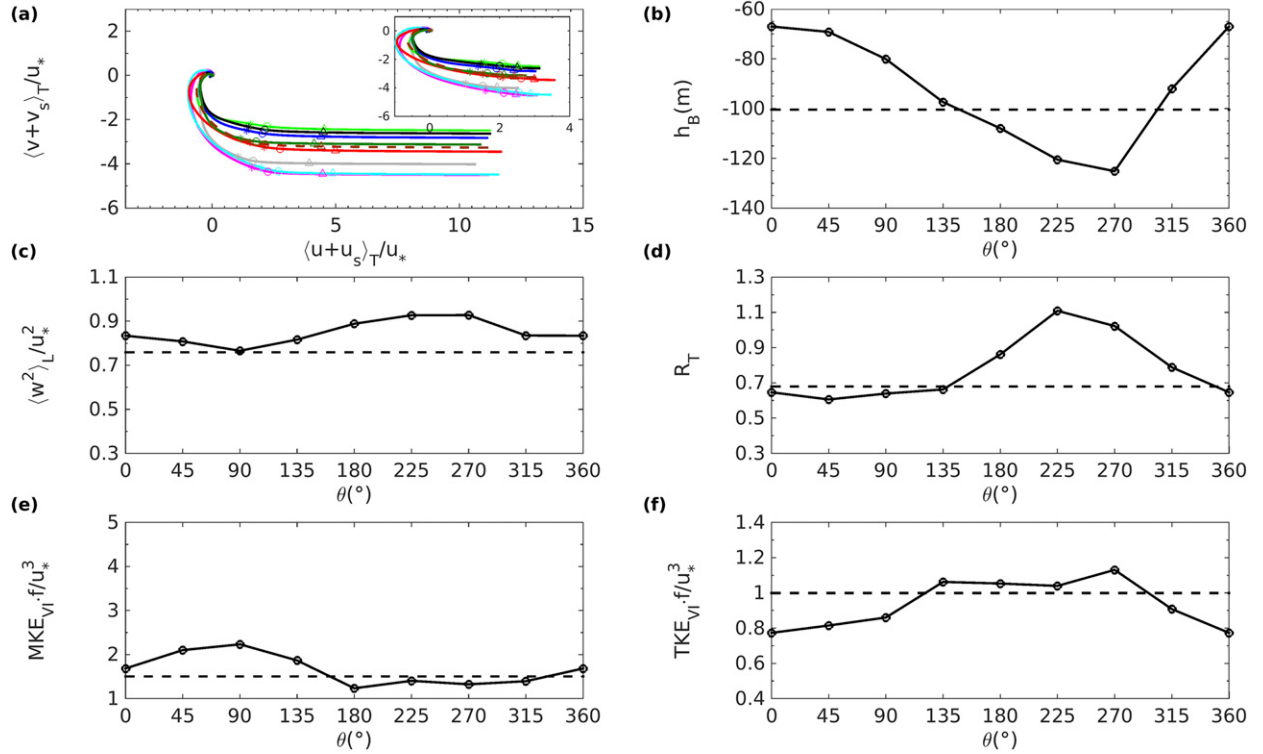


FIG. 11. As in Fig. 3, but effects of wind direction θ on unstratified Langmuir turbulence at 15°N.

The amplitude of the Eulerian current decreases dramatically due to wind-following waves (inset of Fig. 11a), consistent with the Stokes–Ekman theory (e.g., McWilliams et al. 1997). However, the difference in the surface Lagrangian current ($U_0 + u_s$) is slight for cases $180^\circ \leq \theta \leq 270^\circ$, compared with the $f_h = 0$ case. The hodographs with $0^\circ \leq \theta \leq 90^\circ$ deviate from the $f_h = 0$ case, compared with cases $180^\circ \leq \theta \leq 270^\circ$ (Fig. 11a). The difference of maximum and minimum in the angle between surface Eulerian mean current and wind stress is 19.3°, while the difference is 9.5° in the angle between surface Lagrangian mean current and wind stress (not shown).

The boundary layer is deeper in Langmuir turbulence than in Ekman turbulence (Fig. 3b), consistent with previous studies (e.g., McWilliams et al. 2012). The difference in h_B between Ekman and Langmuir simulations for the same wind direction ranges from 0 to 35 m. The largest h_B is 87% larger than the smallest (Fig. 11b). The largest $\langle w^2 \rangle_L$ is 21% larger than the smallest (Fig. 11c). In contrast, the largest R_T is 83% larger than the smallest (Fig. 11d). The variabilities in MKE_{VI} and TKE_{VI} reduce to 81% and 46%, respectively (Figs. 11e,f).

Shear production decreases by 73% in unstratified Langmuir cases with $f_h = 0$, compared to their Ekman counterpart, due to the reduced shear of the Eulerian

mean flow. The largest shear production is about 138% that of the smallest. The reduction in mean velocity (shear) is also due to the Stokes–Coriolis forcing. Although Stokes production ($-\langle u'_j w \rangle \partial \langle u_j^S \rangle / \partial z$) can be nearly 3 times as large as shear production, the differences of Stokes production among different wind directions are negligible. The variability in TKE production with wind direction is mainly determined by Eulerian shear production in unstratified Langmuir cases (Fig. 12). Wind-following waves increase the magnitude of $\langle \tau_e \rangle_L$ but lower its variability to wind direction (not shown).

e. Modification of the f_h effect by swell

Waves and their associated Stokes drifts align with surface wind stress in the previous subsection. This is also the most common regime adopted in many earlier theoretical (Craik and Leibovich 1976; Leibovich 1983) and LES studies of Langmuir turbulence, assuming waves in equilibrium with the steady wind (Skillingstad and Denbo 1995; McWilliams et al. 1997; Harcourt and D’Asaro 2008). In a realistic ocean, waves seldom align with wind because of the influence of swell and the temporal variability of wind. By analyzing LES solutions driven by systematically varying wind–wave misalignment, Van Roekel et al. (2012) showed that a projected Langmuir number can be used to quantify the

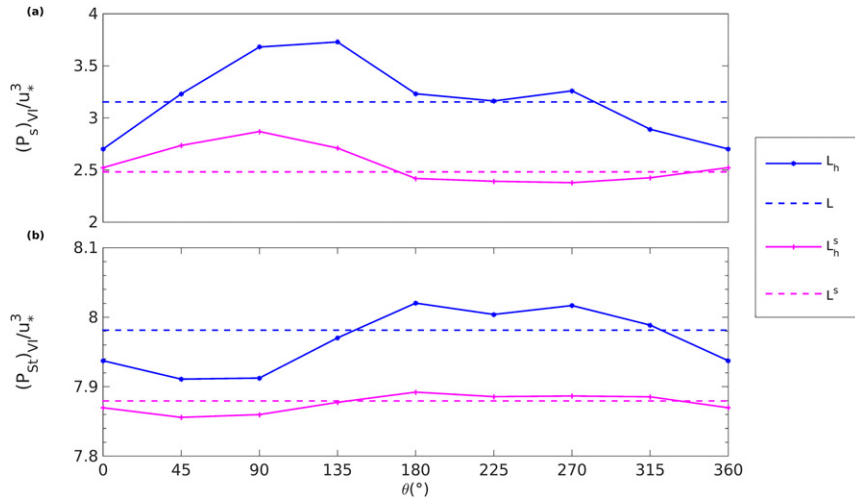


FIG. 12. Impact of wind direction θ on vertically integrated TKE production over boundary (mixed) layer in Langmuir cases without stratification (blue) and with stratification (magenta) at 15°N. (a) Shear production $(P_s)_VI$, normalized by u_*^3 ; (b) Stokes production $(P_{st})_VI$, normalized by u_*^3 . All solid lines indicate results when $f_h \neq 0$, and dashed lines indicate when $f_h = 0$.

strength of Langmuir turbulence with wind–wave misalignment and concluded that as the angle between wind and wave increases, the upwind cell in a Langmuir cell vortex pair becomes stronger than the downwind cell. Recent studies have focused on the relative misalignment of winds and waves, which is critically important in determining the strength of mixing by Langmuir turbulence (Webb and Fox-Kemper 2011; Belcher et al. 2012; Van Roekel et al. 2012). In the regime of wind-opposing swell, Stokes production is negative, leading to smaller turbulence variances (Sullivan et al. 2012) than in Langmuir turbulence. In this study, we consider only two idealized scenarios: the case (S_h) when swell is twice as strong as the equilibrium wave and propagates in the same direction as the wind and the case (M_h) when swell is as strong as equilibrium wave and propagates in the opposite direction as the wind, although wind and wave can be at any angle.

The effect of f_h in Case S_h (Fig. 13) is more similar to Case L_h (section 4d). There is a large decrease in the amplitude of Eulerian mean current in both Case L_h (inset of Fig. 11a) and Case S_h (inset of Fig. 13a). The difference of maximum and minimum in the angle between surface Eulerian mean current and wind stress is 18.4°, while the difference is 4.4° in the angle between surface Lagrangian mean current and wind stress (not shown). The largest boundary layer depth is 128 m when the wind blows westward, while the smallest depth is 71 m when the wind blows northward (Fig. 13b). The relative difference between the largest h_B and the smallest h_B is similar to Case L_h . The largest $\langle w^2 \rangle_L$ is 16% larger than the smallest (Fig. 13c). The variabilities

in R_T , MKE_{VI}, and TKE_{VI} are 80%, 82%, and 47%, respectively (Figs. 13d–f).

The effect of f_h on the pattern of surface vertical velocity fluctuation in Case M_h is negligible as well. Away from the surface ($z/|h_B| < -1/3$), turbulence is more coherent and is of larger spatial scale when the wind blows southward to westward than when the wind blows in other directions. The coherent structures also orient obliquely to wind (not shown), similar to Case E_h .

Compared with the hodograph of the Eulerian mean current with f_h in Case L_h (inset of Fig. 11a), the Eulerian surface mean current with f_h increases due to the negative Stokes drift in the opposite direction of wind in Case M_h (inset of Fig. 14a). The difference of maximum and minimum in the angle between surface Eulerian mean current and wind stress is 7.9°, while the difference is 10.4° in the angle between surface Lagrangian mean current and wind stress (not shown). In comparison with the $f_h = 0$ case driven by wind-following waves (Case L), the boundary layer in Case M ($f_h = 0$) is 30 m shallower due to weaker vertical mixing associated with the negative Stokes drift shear (Fig. 14b). The largest $\langle w^2 \rangle_L$ is 62% larger than the smallest (Fig. 14c). The instantaneous $w(x, y)$ snapshot indicates that the vertical turbulent mixing is stronger when the wind blows southward to westward, represented by coherent streaks of downward velocity (not shown) and deeper boundary layer (not shown). The largest R_T for a southward wind is 99% larger than the smallest for a northward wind (Fig. 14d). The largest MKE_{VI} is 46% larger than the smallest (Fig. 14e). Without the effect of f_h , TKE_{VI} is 31% weaker when a wave propagates in the opposite

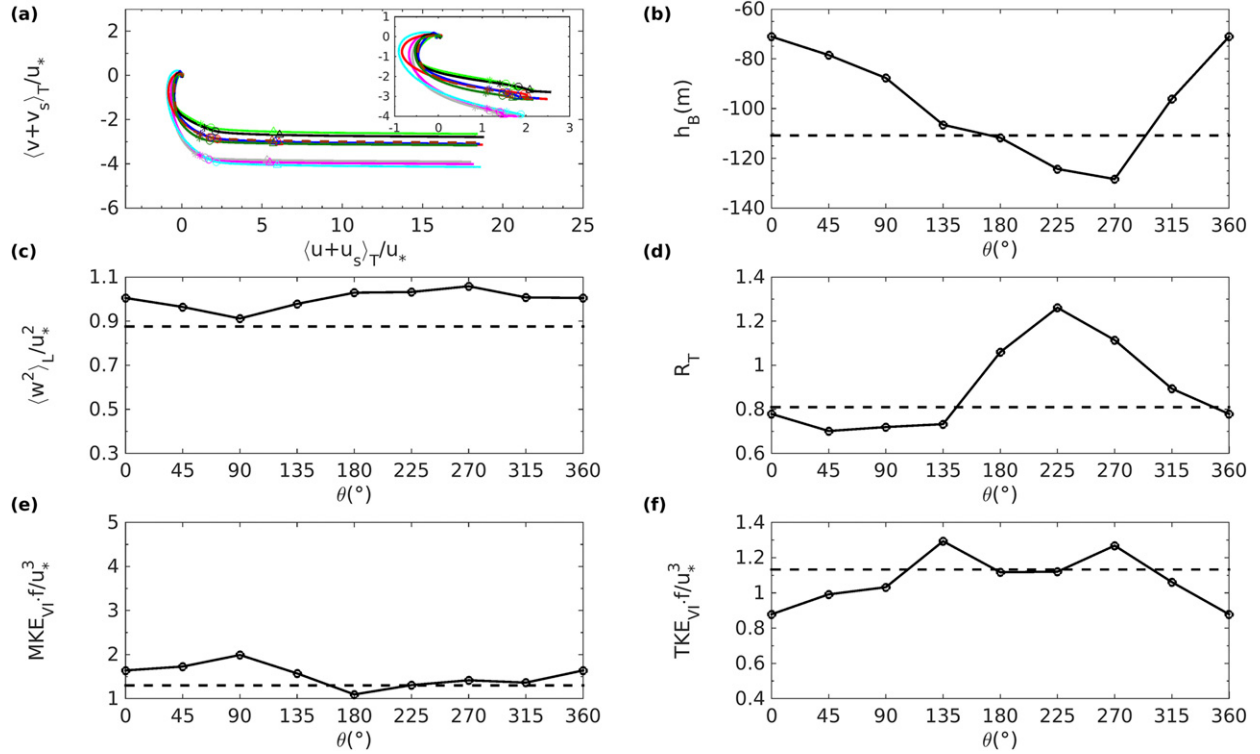


FIG. 13. As in Fig. 3, but for effects of wind direction θ with unstratified swell that is in the same direction as the wind with equilibrium waves at 15°N. The inset is the hodographs for Eulerian mean velocity.

direction of the wind (Fig. 14f) than when a wave is aligned with wind. Under the influence of f_h , the largest TKE_{VI} is 87% larger than the smallest. The effect of f_h when swell is opposite to the wind with equilibrium waves (Fig. 14) is more similar to unstratified Ekman turbulence (section 4a).

f. Modification of f_h effect due to both stratification and waves

Under the simultaneous influence of stratification and nonbreaking surface gravity waves, the variabilities of the mean flow (Fig. 15a) and turbulent statistics to wind direction are small, compared to all other previously discussed cases (Cases E_h , E_h^s , L_h , S_h , and M_h). Wind direction has little effect on the instantaneous flow structure in the stratified Langmuir turbulence since both stratification and Langmuir circulation reduce the variability of turbulent kinetic energy to wind direction (not shown). The difference between the maximum and minimum in the angle between surface Eulerian mean current and wind stress is 2.8°, while the difference is 2.1° for the angle between surface Lagrangian mean current and wind stress.

The magnitude of maximum entrainment rate is 14% larger in stratified Langmuir turbulence (Fig. 15b) than

in stratified Ekman turbulence; however, the ratio of maximum to minimum entrainment rate is similar to that of the stratified Ekman turbulence (Case E_h^s). Equilibrium wave increases w_e by only 3% when $f_h = 0$ (dashed lines in Figs. 9g, 15b), while the variability due to wind direction is similar with and without wave forcing. The boundary layer depth is limited by stratification, similar as the result in section 4c. The layer-averaged $\langle w^2 \rangle_L$ ranges from 0.68 to 0.74 (Fig. 15c), consistent with Harcourt and D'Asaro (2008) and Van Roekel et al. (2012) for simulations with similar parameter space. The wind direction dependence of R_T (Fig. 15d), MKE_{VI} (Fig. 15e), and TKE_{VI} (Fig. 15f) is reduced and even negligible.

The effect of f_h with stratification and wind-opposing swell (Case M_h^s) is similar to the case with stratified Ekman turbulence (Case E_h^s ; see section 4c), and the f_h effect with stratification and wind-following swell (Case S_h^s) is similar to stratified Langmuir turbulence (Case L_h^s).

5. Effect of f_h on eddy viscosity profiles

The effect of turbulence is represented by eddy viscosity K in predictive ocean and climate models.

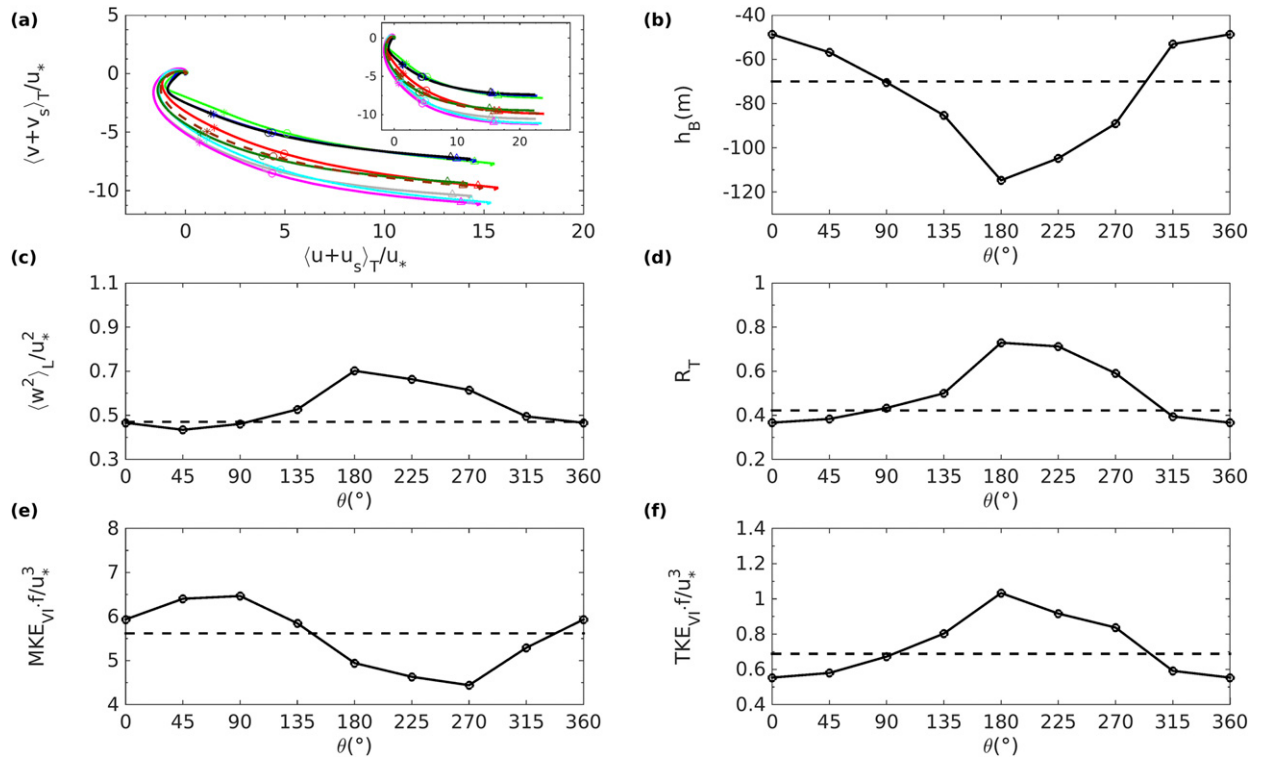


FIG. 14. As in Fig. 13, but for unstratified swell that is in the opposing direction as the wind with equilibrium waves at 15°N.

The LES solutions are used to study the effect of f_h on K in this section. Eddy viscosity is diagnosed as (McWilliams et al. 2012)

$$K = \frac{|\langle u' w \rangle|}{|\partial_z \langle u_\parallel^L \rangle|}, \quad (10)$$

where $\langle u' w \rangle$ is the Reynolds stress, and $\langle u_\parallel^L \rangle = \langle u_\parallel \rangle + \langle u_\parallel^{St} \rangle$ is the Lagrangian mean velocity. The subscript \parallel denotes the horizontal components. The effects of f_h on eddy viscosity profiles in both stratified Ekman and Langmuir cases (Cases E_h^s and L_h^s) at 15°N are shown in Fig. 16. Here, eddy viscosity K is normalized by $u_* |h_M|$ ($|h_M| \sim 45$ m). The impact of f_h on the K profiles is significant, and the value of K changes with wind direction.

For stratified Ekman turbulence, the maximum value of eddy viscosity K_{\max} changes with wind direction (Fig. 16a). The value of K_{\max} is the largest in stratified Ekman turbulence when the wind blows westward ($\theta = 270^\circ$), while it is the smallest when the wind blows northeastward ($\theta = 45^\circ$). The shape of the K profile and the depth where $K = K_{\max}$ are similar for different wind directions ($-0.4 < z/|h_M| < -0.2$). The eddy viscosity reduces to zero at the lower 10% of the mixed layer. The eddy viscosity magnitudes when $0^\circ \leq \theta \leq 90^\circ$ are smaller

than when $f_h = 0$, while those of the opposite wind directions ($180^\circ \leq \theta \leq 270^\circ$) are larger than when $f_h = 0$.

There are two major effects of f_h on K in stratified Langmuir cases. One is the amplification or reduction of the magnitude of K_{\max} : the maximum eddy viscosity decreases for $\theta = 0^\circ \sim 135^\circ$ and increases for $\theta = 180^\circ \sim 315^\circ$, compared with the $f_h = 0$ case. The other is deepening or shoaling the location where $K = K_{\max}$. In stratified Ekman cases, however, the latter effect is negligible.

For stratified Langmuir turbulence, the magnitude of K increases as surface gravity waves enhance turbulent mixing in the mixed layer (Fig. 16b). The value of K_{\max} is the largest for westward wind ($\theta = 270^\circ$), approximately 150% as large as the smallest for eastward wind ($\theta = 90^\circ$). The location of K_{\max} is deeper when K_{\max} is larger, and vice versa. The variation of eddy viscosity profiles with respect to wind direction mainly appears in the middle of the mixed layer ($0.1 \leq z/|h_M| \leq 0.7$). The difference in K profiles is negligibly small ($\sim 6\%$) close to the surface in the stratified Langmuir case, while the largest value of K for a westward wind is twice as large as the smallest value for a northeastward wind in the stratified Ekman case in the upper 10% of the mixed layer. Therefore, the effects of f_h on turbulent mixing are mainly confined to the center of the mixed layer in

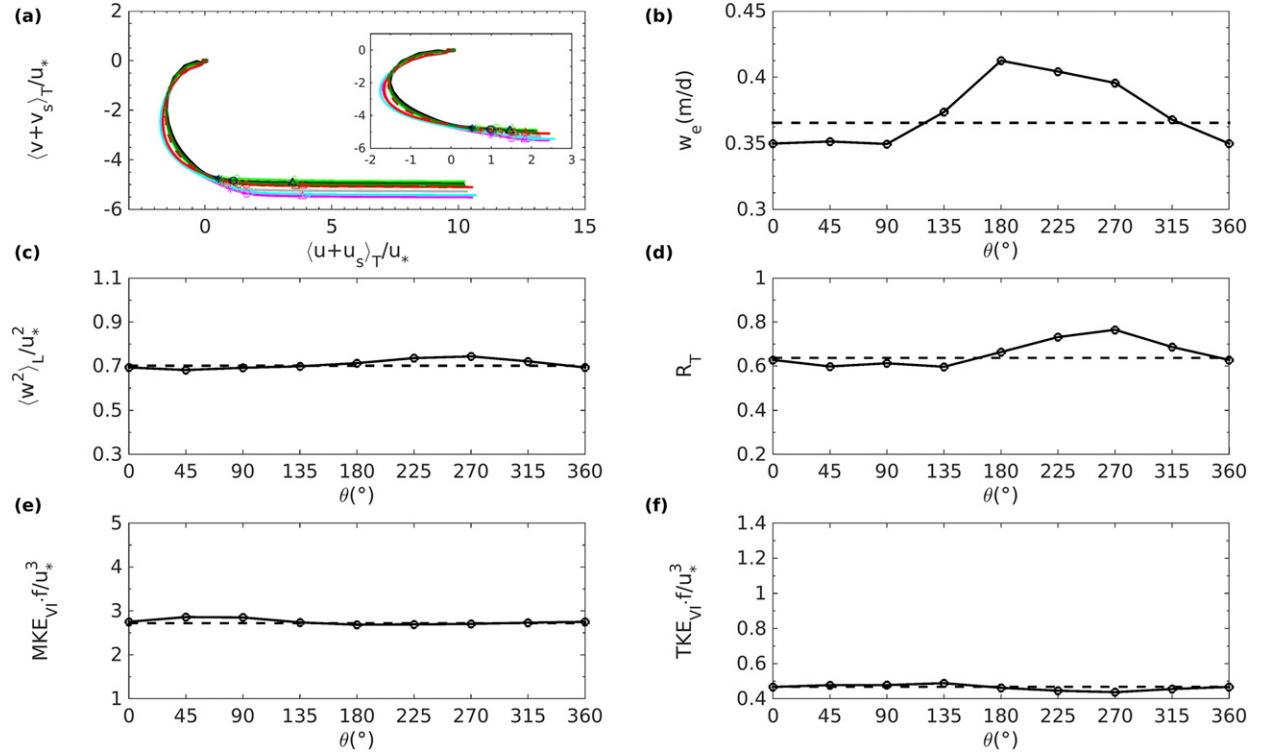


FIG. 15. Effects of wind direction θ on stratified Langmuir turbulence at 15°N. (a) Mean velocity hodographs with symbols indicating different depths: -1 (triangle), -5 (circle), and -10 m (asterisk), and the inset is Eulerian mean velocity hodographs; the line color convention is the same as in Fig. 3a. (b) Entrainment rate w_e (m day^{-1}); (c) layer-averaged variance of vertical velocity $\langle w^2 \rangle_L$, normalized by u_*^2 ; (d) the ratio of vertical component to horizontal component of TKE $R_T = 2\langle w^2 \rangle_L / (\langle u^2 \rangle_L + \langle v^2 \rangle_L)$; (e) Vertically integrated MKE over the mixed layer $\text{MKE}_{VI} = 1/2 \int_{h_M}^0 (\langle u^2 \rangle + \langle v^2 \rangle) dz$, normalized by u_*^3/f ; (f) vertically integrated total (resolved + SGS) turbulent kinetic energy over the mixed layer $\text{TKE}_{VI} = \int_{h_M}^0 [1/2(\langle u^2 \rangle + \langle v^2 \rangle + \langle w^2 \rangle) + \langle e \rangle] dz$, normalized by u_*^3/f . All solid lines indicate results when $f_h \neq 0$, and dashed lines indicate when $f_h = 0$.

stratified Langmuir turbulence. The differences of viscosity with respect to wind direction become more pronounced in stratified Langmuir turbulence, compared to stratified Ekman turbulence.

In the absence of stratification, the K profiles deviate from the convex shape (not shown), consistent with McWilliams et al. (2012). However, there is still a wind direction dependence of eddy viscosity in both unstratified Ekman and Langmuir turbulence, similar to the stratified case (not shown).

A complete mixing parameterization includes boundary layer depth h_B and entrainment rate w_e , in addition to eddy viscosity K . Results in section 4 (Figs. 3, 9, 15) show that the two quantities (h_B and w_e) also change with wind direction when f_h is considered. The evaluation of the existing parameterization for eddy viscosities and the inclusion of the f_h effect in mixing parameterizations are important in improving the performance of parameterizing turbulent mixing in ocean models and will be discussed in a future work.

6. Summary and discussion

In this study, we use large-eddy simulations to investigate how latitude/hemisphere, surface gravity waves, and stratification influence the effect of f_h on OSBL turbulence. In the absence of stable stratification and non-breaking waves, both the mean and turbulent flows change substantially with wind direction and latitude under the influence of f_h , consistent with previous studies (Coleman et al. 1990; Zikanov et al. 2003). Horizontal rotation f_h changes the flow structures and redistributes TKE among three spatial directions. The wind direction dependence of vertically integrated TKE over boundary layer (TKE_{VI}) is mainly determined by the eddy turnover time (or dissipation length scale) instead of TKE production. The variability of turbulent flows to wind direction is different at the same latitude in opposite hemispheres and is also different at different latitudes in the same hemisphere. In the Northern Hemisphere, turbulence is stronger when the wind has a westward and southward component than when the wind has an

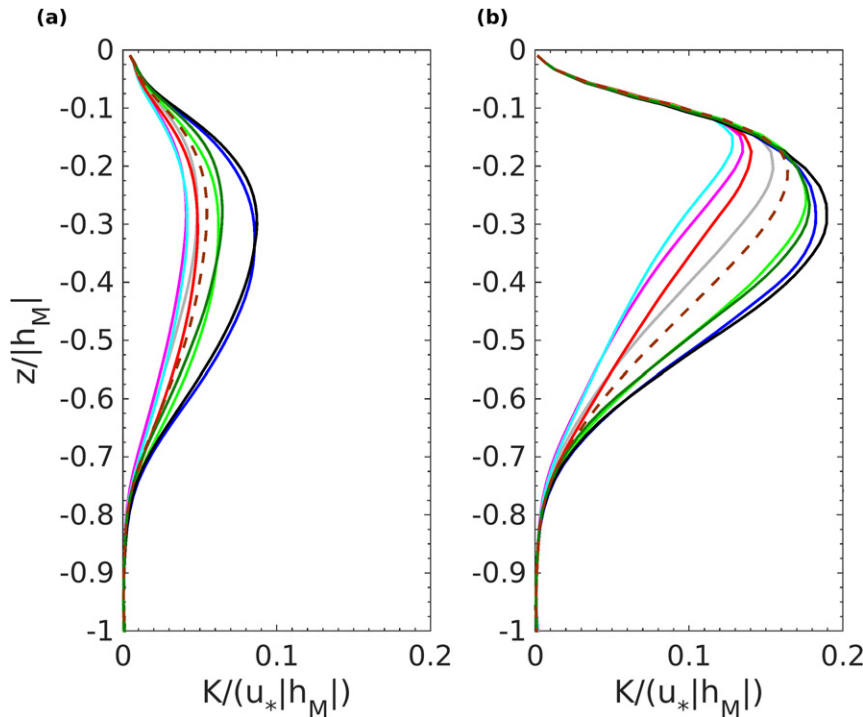


FIG. 16. Comparison of profiles of eddy viscosity K for stratified (left) Ekman and (right) Langmuir cases with respect to wind direction θ at 15°N: $\theta = 0^\circ$ (gray), $\theta = 45^\circ$ (magenta), $\theta = 90^\circ$ (light blue), $\theta = 135^\circ$ (red), $\theta = 180^\circ$ (light green), $\theta = 225^\circ$ (dark blue), $\theta = 270^\circ$ (black), $\theta = 315^\circ$ (dark green), and $f_h = 0$ (brown dashed). Values are normalized by $u_*|h_M|$ for the diagnosis from LES solutions.

eastward and northward component. In the Southern Hemisphere, turbulence is stronger when the wind has a westward and northward component than when the wind has an eastward and southward component. When the boundary layer is capped by stable stratification, f_h alters the entrainment rate and also redistributes TKE among three spatial directions. Both the entrainment rate and the magnitude of eddy viscosity show strong variability with wind direction in stratified Ekman turbulence at 15°N.

Both locally wind-driven wave and swells reduce the wind direction dependence of mean current. However, there are also strong variabilities in both the magnitude and shape of eddy viscosity in the presence of stratification and Langmuir circulations. Wind-opposing swell decreases the wind direction dependence of mean velocity but increases the wind direction dependence of TKE_{VI} .

While f_h has its largest value and effect on turbulence in the tropics, Wang et al. (1996) found that the entraining boundary layer, which is the focus of this study, lacks an equilibrium solution at the equator where f is zero unless large-scale equatorial circulation is included. Furthermore, Wang (2006) also showed that f_h has little

effect on convective turbulence. Therefore, convective turbulence is not discussed in this study.

Accurate simulation of sea surface temperature (SST) and MLD is important to the fidelity of Earth system models and remains one of the major challenges. Recent efforts aiming to reduce existing biases in SST and MLD have focused mainly on the inclusion of parameterization for submesoscale processes (Fox-Kemper et al. 2008; Fox-Kemper and Ferrari 2008; Fox-Kemper et al. 2011) and on the improvement of parameterization for boundary layer mixing by including wave effects (e.g., Qiao et al. 2004; Harcourt 2013, 2015; Fan et al. 2014; Li et al. 2016; Li and Fox-Kemper 2017). These efforts have achieved success to different degrees, but have not fully resolved the biases. The current study demonstrates that the effect of wind direction leads to variability in mixing and associated SST and MLD. For example, in trade wind regions, the northeast wind in the Northern Hemisphere and southeast wind in the Southern Hemisphere drive stronger vertical mixing with f_h than without f_h . In the Bay of Bengal and the Arabian Sea, influenced by Indian monsoon, northeast wind in the winter drives stronger mixing than southwest wind in the summer does if hydrographic conditions are identical.

The difference between the minimum and maximum $\langle w^2 \rangle_L / u_*^2$ is 0.22 in unstratified Ekman turbulence, while $\langle w^2 \rangle_L / u_*^2$ increases from 0.55 in unstratified Ekman turbulence to 0.76 in unstratified Langmuir turbulence at 15°N when $f_h = 0$, indicating that the variability in mixing associated with wind direction is comparable to that due to waves. Normalized maximum eddy viscosity K_{\max} increases from [0.041, 0.087] to [0.129, 0.190] when equilibrium wave is added, while the variabilities in K_{\max} are 110% and 48% for stratified Ekman and Langmuir turbulence, respectively (Figs. 16a,b). The entrainment rate w_e is only 3% larger in wave-driven Langmuir turbulence than in Ekman turbulence. The difference in w_e caused by equilibrium wave forcing is substantially smaller than the variability of w_e to wind direction (~20%). Although the relative importance of wave and wind direction changes with latitude, mixed layer depth, and swell, our results show that wind direction is an important yet overlooked uncertainty in existing ocean vertical mixing parameterization. Inclusion of the wind direction effect in the K -profile parameterization is ongoing and will be reported in a future manuscript.

Acknowledgments. JL and JHL were supported by the National Science Foundation (NSF) through Grants OCE1521018 and CCF1539567. JCM and PPS were supported by the Office of Naval Research through Grant N000141410626. YF was funded under the Naval Research Laboratory base program BE031-03-42-1G35. QC was supported by NSF through Grant CCF1539567. Computations were performed using supercomputing facilities at Louisiana State University, at Louisiana Optical Network Infrastructure (LONI), and at the National Center for Atmospheric Research (NCAR). NCAR is sponsored by NSF.

p	Pressure
P_s	Shear production
P_{St}	Stokes production
P_w	Time rate of wind work
u, v, w	Velocity component
$\langle u'w \rangle, \langle v'w \rangle$	Horizontally averaged vertical momentum flux
u^{St}, v^{St}	Stokes drift
u_s	Stokes drift at the center of the first vertical grid cell along x direction
u_*	Waterside friction velocity
$\langle u_{ }^L \rangle$	Lagrangian mean velocity
U_0, V_0	Mean surface current
w_e	Entrainment rate
β	Angle between surface current and wind stress
ϵ	Dissipation rate
λ_ϵ	Dissipation length scale
φ	Latitude
Ω	Angular speed of Earth's rotation
ω	Vorticity
θ	Wind direction
Θ	Potential temperature
π	Generalized pressure
$\hat{\rho}_0$	Reference density of water
ρ_w	Water density
τ	Wind stress
τ_e	Eddy turnover time
τ_{ij}	Subgrid-scale momentum fluxes
$\tilde{\sigma}$	Radial frequency
$\langle \dots \rangle$	Average over horizontal domain
$\langle \dots \rangle_T$	Average over horizontal domain and time
$\langle \dots \rangle_L$	Layer averaged
X_{VI}	Vertically integrated variable X over the boundary layer

APPENDIX

List of Symbols

f_h	Horizontal component of planetary rotation
f_{hx}, f_{hy}	f_h projected in the x and y directions, respectively
f	Vertical component of planetary rotation
g	Gravitational acceleration
h_B	Boundary layer depth
h_M	Mixed layer depth
F	Wave spectrum
La	Langmuir number
K	Eddy viscosity
K_{\max}	Maximum of eddy viscosity

REFERENCES

- Alves, J. H. G., M. L. Banner, and I. R. Young, 2003: Revisiting the Pierson–Moskowitz asymptotic limits for fully developed wind waves. *J. Phys. Oceanogr.*, **33**, 1301–1323, [https://doi.org/10.1175/1520-0485\(2003\)033<1301:RTPALF>2.0.CO;2](https://doi.org/10.1175/1520-0485(2003)033<1301:RTPALF>2.0.CO;2).
- Belcher, S. E., and Coauthors, 2012: A global perspective on Langmuir turbulence in the ocean surface boundary layer. *Geophys. Res. Lett.*, **39**, L18605, <https://doi.org/10.1029/2012GL052932>.
- Brunner, K., T. Kukulka, G. Proskurowski, and K. Law, 2015: Passive buoyant tracers in the ocean surface boundary layer: 2. Observations and simulations of microplastic marine debris. *J. Geophys. Res. Oceans*, **120**, 7559–7573, <https://doi.org/10.1002/2015JC010840>.
- Coleman, G. N., J. Ferziger, and P. Spalart, 1990: A numerical study of the turbulent Ekman layer. *J. Fluid Mech.*, **213**, 313–348, <https://doi.org/10.1017/S0022112090002348>.

- Craik, A. D., and S. Leibovich, 1976: A rational model for Langmuir circulations. *J. Fluid Mech.*, **73**, 401–426, <https://doi.org/10.1017/S0022112076001420>.
- D'Asaro, E. A., 2014: Turbulence in the upper-ocean mixed layer. *Annu. Rev. Mar. Sci.*, **6**, 101–115, <https://doi.org/10.1146/annurev-marine-010213-135138>.
- , J. Thomson, A. Shcherbina, R. Harcourt, M. Cronin, M. Hemer, and B. Fox-Kemper, 2014: Quantifying upper ocean turbulence driven by surface waves. *Geophys. Res. Lett.*, **41**, 102–107, <https://doi.org/10.1002/2013GL058193>.
- Davidson, P., 2015: *Turbulence: An Introduction for Scientists and Engineers*. Oxford University Press, 630 pp.
- Donelan, M. A., J. Hamilton, and W. Hui, 1985: Directional spectra of wind-generated waves. *Philos. Trans. Roy. Soc. London, 315A*, 509–562, <https://doi.org/10.1098/rsta.1985.0054>.
- Ekman, V., 1905: On the influence of the earth's rotation on ocean-currents. *Ark. Mat. Astron. Fys.*, **2**, 1–53.
- Etlings, D., and F. Wippermann, 1975: On the instability of a planetary boundary layer with Rossby-number similarity. *Bound.-Layer Meteor.*, **9**, 341–360, <https://doi.org/10.1007/BF00230775>.
- Fan, Y., S.-J. Lin, S. M. Griffies, and M. A. Hemer, 2014: Simulated global swell and wind-sea climate and their responses to anthropogenic climate change at the end of the twenty-first century. *J. Climate*, **27**, 3516–3536, <https://doi.org/10.1175/JCLI-D-13-00198.1>.
- Farmer, D., and M. Li, 1995: Patterns of bubble clouds organized by Langmuir circulation. *J. Phys. Oceanogr.*, **25**, 1426–1440, [https://doi.org/10.1175/1520-0485\(1995\)025<1426:POBCOB>2.0.CO;2](https://doi.org/10.1175/1520-0485(1995)025<1426:POBCOB>2.0.CO;2).
- Fer, I., 2006: Scaling turbulent dissipation in an Arctic fjord. *Deep-Sea Res. II*, **53**, 77–95, <https://doi.org/10.1016/j.dsr.2006.01.003>.
- Fox-Kemper, B., and R. Ferrari, 2008: Parameterization of mixed layer eddies. Part II: Prognosis and impact. *J. Phys. Oceanogr.*, **38**, 1166–1179, <https://doi.org/10.1175/2007JPO3788.1>.
- , —, and R. Hallberg, 2008: Parameterization of mixed layer eddies. Part I: Theory and diagnosis. *J. Phys. Oceanogr.*, **38**, 1145–1165, <https://doi.org/10.1175/2007JPO3792.1>.
- , —, and Coauthors, 2011: Parameterization of mixed layer eddies. III: Implementation and impact in global ocean climate simulations. *Ocean Modell.*, **39**, 61–78, <https://doi.org/10.1016/j.ocemod.2010.09.002>.
- Galperin, B., L. Kantha, G. Mellor, and A. Rosati, 1989: Modeling rotating stratified turbulent flows with application to oceanic mixed layers. *J. Phys. Oceanogr.*, **19**, 901–916, [https://doi.org/10.1175/1520-0485\(1989\)019<0901:MRSTFW>2.0.CO;2](https://doi.org/10.1175/1520-0485(1989)019<0901:MRSTFW>2.0.CO;2).
- Gargett, A., J. Wells, A. Tejada-Martinez, and C. Grosch, 2004: Langmuir supercells: A mechanism for sediment resuspension and transport in shallow seas. *Science*, **306**, 1925–1928, <https://doi.org/10.1126/science.1100849>.
- Garwood, R. W., Jr., P. C. Gallacher, and P. Muller, 1985a: Wind direction and equilibrium mixed layer depth: General theory. *J. Phys. Oceanogr.*, **15**, 1325–1331, [https://doi.org/10.1175/1520-0485\(1985\)015<1325:WDAEML>2.0.CO;2](https://doi.org/10.1175/1520-0485(1985)015<1325:WDAEML>2.0.CO;2).
- , P. Muller, and P. C. Gallacher, 1985b: Wind direction and equilibrium mixed layer depth in the tropical Pacific Ocean. *J. Phys. Oceanogr.*, **15**, 1332–1338, [https://doi.org/10.1175/1520-0485\(1985\)015<1332:WDAEML>2.0.CO;2](https://doi.org/10.1175/1520-0485(1985)015<1332:WDAEML>2.0.CO;2).
- Grant, A. L., and S. E. Belcher, 2009: Characteristics of Langmuir turbulence in the ocean mixed layer. *J. Phys. Oceanogr.*, **39**, 1871–1887, <https://doi.org/10.1175/2009JPO4119.1>.
- Hamlington, P. E., L. P. Van Roekel, B. Fox-Kemper, K. Julien, and G. P. Chini, 2014: Langmuir-submesoscale interactions: Descriptive analysis of multiscale frontal spindown simulations. *J. Phys. Oceanogr.*, **44**, 2249–2272, <https://doi.org/10.1175/JPO-D-13-0139.1>.
- Harcourt, R. R., 2013: A second-moment closure model of Langmuir turbulence. *J. Phys. Oceanogr.*, **43**, 673–697, <https://doi.org/10.1175/JPO-D-12-0105.1>.
- , 2015: An improved second-moment closure model of Langmuir turbulence. *J. Phys. Oceanogr.*, **45**, 84–103, <https://doi.org/10.1175/JPO-D-14-0046.1>.
- , and E. A. D'Asaro, 2008: Large-eddy simulation of Langmuir turbulence in pure wind seas. *J. Phys. Oceanogr.*, **38**, 1542–1562, <https://doi.org/10.1175/2007JPO3842.1>.
- Hassid, S., and B. Galperin, 1994: Modeling rotating flows with neutral and unstable stratification. *J. Geophys. Res.*, **99**, 12 533–12 548, <https://doi.org/10.1029/94JC00149>.
- Kantha, L. H., A. Rosati, and B. Galperin, 1989: Effect of rotation on vertical mixing and associated turbulence in stratified fluids. *J. Geophys. Res.*, **94**, 4843–4854, <https://doi.org/10.1029/JC094iC04p04843>.
- Klemp, J. B., and D. R. Durran, 1983: An upper boundary condition permitting internal gravity wave radiation in numerical meso-scale models. *Mon. Wea. Rev.*, **111**, 430–444, [https://doi.org/10.1175/1520-0493\(1983\)111<0430:AUBCPI>2.0.CO;2](https://doi.org/10.1175/1520-0493(1983)111<0430:AUBCPI>2.0.CO;2).
- Kukulka, T., and K. Brunner, 2015: Passive buoyant tracers in the ocean surface boundary layer: 1. Influence of equilibrium wind-waves on vertical distributions. *J. Geophys. Res. Oceans*, **120**, 3837–3858, <https://doi.org/10.1002/2014JC010487>.
- , A. J. Plueddemann, J. H. Trowbridge, and P. P. Sullivan, 2010: Rapid mixed layer deepening by the combination of Langmuir and shear instabilities: A case study. *J. Phys. Oceanogr.*, **40**, 2381–2400, <https://doi.org/10.1175/2010JPO4403.1>.
- , —, —, and —, 2011: The influence of crosswind tidal currents on Langmuir circulation in a shallow ocean. *J. Geophys. Res.*, **116**, C08005, <https://doi.org/10.1029/2011JC006971>.
- , K. L. Law, and G. Proskurowski, 2016: Evidence for the influence of surface heat fluxes on turbulent mixing of microplastic marine debris. *J. Phys. Oceanogr.*, **46**, 809–815, <https://doi.org/10.1175/JPO-D-15-0242.1>.
- Langmuir, I., 1938: Surface motion of water induced by wind. *Science*, **87**, 119–123, <https://doi.org/10.1126/science.87.2250.119>.
- Leibovich, S., 1983: The form and dynamics of Langmuir circulations. *Annu. Rev. Fluid Mech.*, **15**, 391–427, <https://doi.org/10.1146/annurev.fl.15.010183.002135>.
- , and S. Lele, 1985: The influence of the horizontal component of Earth's angular velocity on the instability of the Ekman layer. *J. Fluid Mech.*, **150**, 41–87, <https://doi.org/10.1017/S002211208500039>.
- Li, M., C. Garrett, and E. Skillingstad, 2005: A regime diagram for classifying turbulent large eddies in the upper ocean. *Deep-Sea Res. I*, **52**, 259–278, <https://doi.org/10.1016/j.dsr.2004.09.004>.
- Li, Q., and B. Fox-Kemper, 2017: Assessing the effects of Langmuir turbulence on the entrainment buoyancy flux in the ocean surface boundary layer. *J. Phys. Oceanogr.*, **47**, 2863–2886, <https://doi.org/10.1175/JPO-D-17-0085.1>.
- , A. Webb, B. Fox-Kemper, A. Craig, G. Danabasoglu, W. G. Large, and M. Vertenstein, 2016: Langmuir mixing effects on global climate: WAVEWATCH III in CESM. *Ocean Modell.*, **103**, 145–160, <https://doi.org/10.1016/j.ocemod.2015.07.020>.
- Liang, J.-H., J. C. McWilliams, P. P. Sullivan, and B. Baschek, 2011: Modeling bubbles and dissolved gases in the ocean. *J. Geophys. Res.*, **116**, C03015, <https://doi.org/10.1029/2010JC006579>.

- , —, —, and —, 2012: Large eddy simulation of the bubbly ocean: New insights on subsurface bubble distribution and bubble-mediated gas transfer. *J. Geophys. Res.*, **117**, C04002, <https://doi.org/10.1029/2011JC007766>.
- , S. R. Emerson, E. A. D'Asaro, C. L. McNeil, R. R. Harcourt, P. P. Sullivan, B. Yang, and M. F. Cronin, 2017: On the role of sea-state in bubble-mediated air-sea gas flux during a winter storm. *J. Geophys. Res. Oceans*, **122**, 2671–2685, <https://doi.org/10.1002/2016JC012408>.
- Liu, W. T., K. B. Katsaros, and J. A. Businger, 1979: Bulk parameterization of air-sea exchanges of heat and water vapor including the molecular constraints at the interface. *J. Atmos. Sci.*, **36**, 1722–1735, [https://doi.org/10.1175/1520-0469\(1979\)036<1722:BPOASE>2.0.CO;2](https://doi.org/10.1175/1520-0469(1979)036<1722:BPOASE>2.0.CO;2).
- McWilliams, J. C., and J. M. Restrepo, 1999: The wave-driven ocean circulation. *J. Phys. Oceanogr.*, **29**, 2523–2540, [https://doi.org/10.1175/1520-0485\(1999\)029<2523:TWDOC>2.0.CO;2](https://doi.org/10.1175/1520-0485(1999)029<2523:TWDOC>2.0.CO;2).
- , and E. Huckle, 2006: Ekman layer rectification. *J. Phys. Oceanogr.*, **36**, 1646–1659, <https://doi.org/10.1175/JPO2912.1>.
- , P. P. Sullivan, and C.-H. Moeng, 1997: Langmuir turbulence in the ocean. *J. Fluid Mech.*, **334**, 1–30, <https://doi.org/10.1017/S0022112096004375>.
- , E. Huckle, J.-H. Liang, and P. P. Sullivan, 2012: The wavy Ekman layer: Langmuir circulations, breaking waves, and Reynolds stress. *J. Phys. Oceanogr.*, **42**, 1793–1816, <https://doi.org/10.1175/JPO-D-12-071.1>.
- , —, —, and —, 2014: Langmuir turbulence in swell. *J. Phys. Oceanogr.*, **44**, 870–890, <https://doi.org/10.1175/JPO-D-13-0122.1>.
- Mellor, G. L., and T. Yamada, 1982: Development of a turbulence closure model for geophysical fluid problems. *Rev. Geophys.*, **20**, 851–875, <https://doi.org/10.1029/RG020i004p00851>.
- Moeng, C., and P. Sullivan, 2002: Large eddy simulation. *Encyclopedia of Atmospheric Sciences*, J. Curry and J. R. Holton, Eds., Academic Press, 1140–1150.
- Monin, A., and A. Obukhov, 1954: Basic laws of turbulent mixing in the surface layer of the atmosphere (in Russian). *Tr. Geofiz. Inst., Akad. Nauk SSSR*, **24**, 1963–1967.
- Pearson, B. C., A. L. Grant, J. A. Polton, and S. E. Belcher, 2015: Langmuir turbulence and surface heating in the ocean surface boundary layer. *J. Phys. Oceanogr.*, **45**, 2897–2911, <https://doi.org/10.1175/JPO-D-15-0018.1>.
- Plueddemann, A. J., J. A. Smith, D. M. Farmer, R. A. Weller, W. R. Crawford, R. Pinkel, S. Vagle, and A. Gnanadesikan, 1996: Structure and variability of Langmuir circulation during the Surface Waves Processes Program. *J. Geophys. Res.*, **101**, 3525–3543, <https://doi.org/10.1029/95JC03282>.
- Polton, J. A., D. M. Lewis, and S. E. Belcher, 2005: The role of wave-induced Coriolis–Stokes forcing on the wind-driven mixed layer. *J. Phys. Oceanogr.*, **35**, 444–457, <https://doi.org/10.1175/JPO2701.1>.
- Price, J. F., and M. A. Sundermeyer, 1999: Stratified Ekman layers. *J. Geophys. Res.*, **104**, 20 467–20 494, <https://doi.org/10.1029/1999JC900164>.
- , C. N. Mooers, and J. C. Van Leer, 1978: Observation and simulation of storm-induced mixed-layer deepening. *J. Phys. Oceanogr.*, **8**, 582–599, [https://doi.org/10.1175/1520-0485\(1978\)008<0582:OASOSI>2.0.CO;2](https://doi.org/10.1175/1520-0485(1978)008<0582:OASOSI>2.0.CO;2).
- Qiao, F., Y. Yuan, Y. Yang, Q. Zheng, C. Xia, and J. Ma, 2004: Wave-induced mixing in the upper ocean: Distribution and application to a global ocean circulation model. *Geophys. Res. Lett.*, **31**, L11303, <https://doi.org/10.1029/2004GL019824>.
- Rossby, C.-G., and R. B. Montgomery, 1935: The layer of frictional influence in wind and ocean currents. *Pap. Phys. Oceanogr. Meteor.*, **3**, 1–101, <https://doi.org/10.1575/1912/1157>.
- Sanford, T. B., J. F. Price, and J. B. Girton, 2011: Upper-ocean response to Hurricane Frances (2004) observed by profiling EM-APEX floats. *J. Phys. Oceanogr.*, **41**, 1041–1056, <https://doi.org/10.1175/2010JPO4313.1>.
- Skyllingstad, E. D., and D. W. Denbo, 1995: An ocean large-eddy simulation of Langmuir circulations and convection in the surface mixed layer. *J. Geophys. Res.*, **100**, 8501–8522, <https://doi.org/10.1029/94JC03202>.
- Smith, J. A., 1992: Observed growth of Langmuir circulation. *J. Geophys. Res.*, **97**, 5651–5664, <https://doi.org/10.1029/91JC03118>.
- Smith, K. M., P. E. Hamlington, and B. Fox-Kemper, 2016: Effects of submesoscale turbulence on ocean tracers. *J. Geophys. Res. Oceans*, **121**, 908–933, <https://doi.org/10.1002/2015JC01108>.
- Sullivan, P. P., and J. C. McWilliams, 2010: Dynamics of winds and currents coupled to surface waves. *Annu. Rev. Fluid Mech.*, **42**, 19–42, <https://doi.org/10.1146/annurev-fluid-121108-145541>.
- , —, and C.-H. Moeng, 1994: A subgrid-scale model for large-eddy simulation of planetary boundary-layer flows. *Bound.-Layer Meteor.*, **71**, 247–276, <https://doi.org/10.1007/BF00713741>.
- , —, and —, 1996: A grid nesting method for large-eddy simulation of planetary boundary-layer flows. *Bound.-Layer Meteor.*, **80**, 167–202, <https://doi.org/10.1007/BF00119016>.
- , C.-H. Moeng, B. Stevens, D. H. Lenschow, and S. D. Mayor, 1998: Structure of the entrainment zone capping the convective atmospheric boundary layer. *J. Atmos. Sci.*, **55**, 3042–3064, [https://doi.org/10.1175/1520-0469\(1998\)055<3042:SOTEZC>2.0.CO;2](https://doi.org/10.1175/1520-0469(1998)055<3042:SOTEZC>2.0.CO;2).
- , J. C. McWilliams, and W. K. Melville, 2007: Surface gravity wave effects in the oceanic boundary layer: Large-eddy simulation with vortex force and stochastic breakers. *J. Fluid Mech.*, **593**, 405–452, <https://doi.org/10.1017/S002211200700897X>.
- , L. Romero, J. C. McWilliams, and W. K. Melville, 2012: Transient evolution of Langmuir turbulence in ocean boundary layers driven by hurricane winds and waves. *J. Phys. Oceanogr.*, **42**, 1959–1980, <https://doi.org/10.1175/JPO-D-12-025.1>.
- Suzuki, N., and B. Fox-Kemper, 2016: Understanding Stokes forces in the wave-averaged equations. *J. Geophys. Res. Oceans*, **121**, 3579–3596, <https://doi.org/10.1002/2015JC011566>.
- Tejada-Martínez, A., and C. Grosch, 2007: Langmuir turbulence in shallow water. Part 2. Large-eddy simulation. *J. Fluid Mech.*, **576**, 63–108, <https://doi.org/10.1017/S0022112006004587>.
- Tennekes, H., and J. L. Lumley, 1972: *A First Course in Turbulence*. MIT Press, 300 pp.
- Van Roekel, L., B. Fox-Kemper, P. Sullivan, P. Hamlington, and S. Haney, 2012: The form and orientation of Langmuir cells for misaligned winds and waves. *J. Geophys. Res.*, **117**, C05001, <https://doi.org/10.1029/2011JC007516>.
- Wang, D., 2006: Effects of the Earth's rotation on convection: Turbulent statistics, scaling laws and Lagrangian diffusion. *Dyn. Atmos. Oceans*, **41**, 103–120, <https://doi.org/10.1016/j.dynatmoce.2006.01.001>.
- , W. G. Large, and J. C. McWilliams, 1996: Large-eddy simulation of the equatorial ocean boundary layer: Diurnal cycling, eddy viscosity, and horizontal rotation.

- J. Geophys. Res.*, **101**, 3649–3662, <https://doi.org/10.1029/95JC03441>.
- Webb, A., and B. Fox-Kemper, 2011: Wave spectral moments and Stokes drift estimation. *Ocean Model.*, **40**, 273–288, <https://doi.org/10.1016/j.ocemod.2011.08.007>.
- Weller, R. A., and J. F. Price, 1988: Langmuir circulation within the oceanic mixed layer. *Deep-Sea Res.*, **35**, 711–747, [https://doi.org/10.1016/0198-0149\(88\)90027-1](https://doi.org/10.1016/0198-0149(88)90027-1).
- White, A. A., and R. Bromley, 1995: Dynamically consistent, quasi-hydrostatic equations for global models with a complete representation of the Coriolis force. *Quart. J. Roy. Meteor. Soc.*, **121**, 399–418, <https://doi.org/10.1002/qj.49712152208>.
- Zikanov, O., D. N. Slinn, and M. R. Dhanak, 2003: Large-eddy simulations of the wind-induced turbulent Ekman layer. *J. Fluid Mech.*, **495**, 343–368, <https://doi.org/10.1017/S0022112003006244>.